Master's Thesis

Death-associated kinase-related (Drak) localization in *Drosophila* during early embryogenesis

Panu Tapio Siipilehto

University of Jyväskylä

Department of Biological and Environmental Science

11.11.2023

UNIVERSITY OF JYVÄSKYLÄ, Faculty of Mathematics and Science
Department of Biological and Environmental Science
Master's Degree Programme in Cell and Molecular Biology

Siipilehto, Panu T.

Death-associated kinase-related (Drak) localization in *Drosophila* during early embryogenesis

MSci Thesis
43 p., 6 appendices (6 p.)
Supervisors: Prof. Jari Ylänne

Reviewers: Prof. Janne Ihalainen, PhD Visa Ruokolainen

September 2023

Keywords: actin front, MLCK, cellularization, live tissue imaging

Cells can regulate cellular processes by sensing mechanical forces in a process known as mechanotransduction. This can be achieved with cytoskeletal proteins such as actin crosslinking protein filamin. Fruit fly filamin is known as Cheerio (Cher). In this study, I focused on actomyosin regulations during the cellularization phase of *Drosophila* early embryogenesis. Specifically, I studied filamin, myosin regulatory light chain protein called Spaghetti squash (Sqh), and Death-associated kinase-related (Drak). Prior research has shown that filamin and Sqh colocalize during cellularization. Additionally, Drak binds to filamin, and both Drak and filamin are involved in the regulation of cellularization. Drak also phosphorylates Sqh, but its localization during *Drosophila* cellularization is unknown. I used *Drosophila melanogaster* lines that expressed Green fluorescent protein (GFP) or mCherry red fluorescent protein fusions of Cher, Drak, and Sqh. Early embryos were time-lapse imaged with confocal microscopy and analyzed with ImageJ software. Pearson's Correlation Coefficient (PCC) was calculated for selected region-of-interests. The main results showed that a proportion of Drak localizes to actin front together with Cher. Cher and Sqh PCC increased as cellularization progresses. In contrast, Drak and Cher colocalization remained similar throughout. Drak also localized near cellular cortex between nuclear divisions and throughout the cellularization process. My results suggest that Drak may have a role in both the cortical region and in the cellularization front. These results provide further knowledge for characterizing the mechanically regulated signaling pathways of filamin.

JYVÄSKYLÄN YLIOPISTO, Matemaattis-luonnontieteellinen tiedekunta
Bio- ja ympäristötieteiden laitos
Solu- ja molekyylibiologian maisteriohjelma

Siipilehto Panu T.	Solukuolemaan liittyvän kinaasin (Drak) lokalisaatio *Drosophila*-kärpäsellä varhaisen alkionkehityksen aikana
Pro gradu tutkielma:	43 s., 6 liitettä (6 s.)
Työn ohjaajat:	Prof. Jari Ylänne
Tarkastajat:	Prof. Janne Ihalainen, FT Visa Ruokalainen

Syyskuu 2023

Hakusanat: aktiinifrontti, MLCK, varhaisen solujen muodostuminen, elävän kudoksen kuvantaminen

Solut säätelevät monia solun prosesseja aistimalla mekaanisia voimia ja muuttamalla ne biokemiallisiksi signaaleiksi. Yksi tähän osallistuvista proteiineista on aktiinisäikeitä yhteenliittävä filamiini. Banaanikärpäsen filamiini on nimeltään Cheerio (Cher). Tutkimuksessa keskityin aktomyosiinin säätelyyn *Drosophila*-kärpäsen alkion varhaisen solujen muodostumisen aikana. Erityisesti tarkastelin filamiinin, myosiinin säätelyalayksikköä nimeltä Spaghetti squash (Sqh) ja solukuolemaan liittyvää proteiinikinaasin (Drak) lokalisaatioita. Aiemmat tutkimukset ovat osoittaneet, että filamiini yhteislokalisoituu Sqh:n kanssa varhaisen solujen muodostumisen aikana. Lisäksi Drak sitoutuu filamiiniin, ja sekä Drak että filamiini osallistuvat varhaisen solujen muodostumisen säätelyyn. Drak pystyy myös säätelemään Sqh:tä fosforylaation kautta, mutta sen lokalisaatio ei ole tiedossa. Käytin tutkimuksessa *Drosophila melanogaster* -linjoja, jotka ilmaisivat vihreätä fluoresoivaa proteiinia (GFP) tai punaista fluoresoivaa proteiinia (mCherry) Cher:n, Drak:n ja Sqh:n proteiiniyhdisteinä. Varhaiset kärpäsalkiot kuvattiin aikaseurannalla konfokaalimikroskoopilla ja analysoitiin ImageJ -ohjelmalla. Pearsonin kolokalisaatiokerroin (PCC) laskettiin valituille kohdealueille. Tutkimuksen päätulos osoitti, että Drak lokalisoituu osittain aktiinifronttiin Cher:n kanssa. Cher:n ja Sqh:n PCC kasvaa aktiinifrontin edetessä, kun taas Drak:n ja Cher:n välillä se pysyy samana. Drak-signaali lokalisoitui myös lähellä solukerrosrakennetta tumanjakautumisten välillä ja solujen muodostumisen aikana. Tutkimukseni tulokset viittaavat siihen, että Drak-proteiinilla voi olla rooli solukuoren alueella sekä aktiinifrontissa. Nämä tulokset tarjoavat myös lisätietoa filamiinin mekaanisesti säädellyn signaloinnin karakterisoinnista.

TABLE OF CONTENTS

TERMS AND ABBREVIATIONS

Terms

Mechanosensing	Cells ability to sense and respond to a variety of mechanical signals
Mechanotransduction	Conversion of mechanical stimulus to biochemical reaction and a cellular response
Actin front	Specialized structure composed of actin filaments that forms at the leading edge of the cellularization furrow in early stages of embryonic development in *Drosophila.*

Abbreviations

ABD	Actin-binding domain
Cher	Cheerio filamin
Drak	Death-associated protein kinase related
ECM	Extracellular matrix
Ig	Immunoglobulin
MLCK	Myosin light chain kinase
MSR	Mechanosensitive region
NM II	Non-muscle myosin II
PCC	Pearson's Correlation Coefficient
MCC	Mander's Colocalization Coefficient
ROCK (Rok)	Rho-associated protein kinase
Sqh	Spaghetti squash

1 INTRODUCTION

Cell communication with adjacent cells and their surroundings through extracellular matrix (ECM) is central in cell differentiation and regulation of tissue size and shape (Neubueser and Hipfner 2010). Cells are in constant communication to their environment through soluble signal molecules, cell-cell adhesion, and cell-ECM adhesion (Bao and Shuresh 2003). Signal molecule receptors and adhesion receptors can function as signaling receptors directly. Additionally, adhesion receptors can transduce mechanical forces, which cells can detect and lead to various cellular responses (Hoffman et al. 2011, Oria et al. 2017). This is known as mechanosensing. Mechanosensitive macromolecules can function as either cell surface receptors or cell surface ion channels (Vogel and Sheetz 2006). Alternatively, they can be proteins that connect to cell attachment sites through cytoskeleton. One of the family of cytoskeleton-linked mechanosensitive proteins are filamins, which function as an actin cross-linking protein (Nakamura et al. 2011).

The model organisms *Drosophila melanogaster* has been central in studies regarding to dynamic regulation of the actin cytoskeleton and its role in coordinating complex cell shape changes. Morphogenetic changes have been extensively studied during *D. melanogaster* different development stages. For example, during embryogenesis, the fruit fly embryo undergoes a precise series of cell divisions and cellularization that are coordinated by several signaling mechanisms. One of the main drivers for these various morphogenetic cellular processes is myosin, which is central in mechanical force generation (Quentin 2008). Many of these processes are regulated via phosphorylation of myosin, however, much of this signaling pathway is still unknown (Betabudi 2014). Thus, it is with great interest to understand the signaling mechanisms controlling myosin activity and to understand how cell and tissue shape is determined. In this master thesis, the focus is on investigating *D. melanogaster* mechanosensitive macromolecule filamin Cheerio (Cher) and its possible interaction with Death-associated protein kinase-related (Drak), that is known to regulate myosin by phosphorylation (Neubueser and Hipfner 2010). In this study, I employ a colocalization analysis approach to investigate the interactions of these proteins. Colocalization analysis allows the quantification of the proximity between two biological fluorescent molecules. In the introduction sections, I will review *D. melanogaster* early development and cellularization. Secondly, I will discuss filamin Cher and its role in actin crosslinking. Thirdly, I will explore the role of the molecular motor myosin functions and regulation that are central in driving the morphogenetic changes in cellularization. Finally, I will present Drak and its function.

1.1 *Drosophila* embryogenesis

During *Drosophila* embryogenesis, the fertilized egg undergoes a series of nuclear divisions and cell differentiation to develop into a motile larva. This study's main focus was on the early stages of development, where the embryo undergoes cellularization resulting in 6000 blastoderm cells.

Embryogenesis starts with the fertilization of the oocyte, where the haploid nuclei of the sperm and egg fuse together, forming a diploid nucleus (Hales et al. 2015). After fertilization, embryo development begins with nuclear division cycles in a common cytoplasm. In this stage, the embryo is referred to as a syncytial blastoderm (syncytium) (Gilbert 2003, Hales et al. 2015). The embryonic nuclei undergo nine division cycles in the embryo interior and a tenth nuclear cycle, around 80-90 minutes post-fertilization (25 ^{o}C) after nuclei migration and anchoring to the embryo cortex to the monolayer beneath the plasma membrane (Foe and Alberts 1983, Sokac et al. 2022). This is followed by another three nuclear cycles resulting in a monolayer that contains around 6000 nuclei (Gilbert 2003, Sokac et al. 2022).

At the onset of cellularization ("priming phase"), the nuclei are positioned, and new membrane must be formed between each dividing nucleus after nuclear cycle 13 mitosis (~130 min post-fertilization) (Sokac et al. 2022). The nuclei are positioned by microtubule asters, that also determine the furrow positions by a similar mechanism to cytokinesis (Pollard and O'Shaughnessy 2019, Sokac et al. 2022). Between the new two nuclei, non-muscle myosin II (NM II), actin, and many other components are recruited via cytoplasmic flow, called cortical flow (Sokac et al. 2022). This occurs beneath the plasma membrane and is driven by a difference in cell surface tensions where the flow moves from areas of lower cell surface tension to areas of higher tension (Bray and White 1988, Reymann et al. 2016, Sokac et al. 2022). After several minutes of the furrow initiation, actin and NM II accumulates at furrows (Afshar et al. 2000, Minestrini et al. 2003, Großhans et al. 2005, Sokac et al. 2022). Formation of new furrows around every nucleus occurs in four to five minutes (He et al. 2016, Sokac et al. 2022).

After priming phase, true cellularization takes place in four distinct phases, that can also be divided into slow and fast phases (Mazumdar A. and Mazumdar M. 2002). During these phases, cell undergoes rapid surface expansion, increasing plasma membrane area by 25-fold to reach a final cross-sectional length within an hour (Sokac et al. 2022, Lecuit and Wieschaus 2000, Figard et al. 2013). In the beginning, the actin filaments are densely populated in compartments above nuclei, but as cellularization begins, the actin becomes more concentrated at the furrow canals between the nuclei (Warn and Magrath 1990, Mazumdar A. and Mazumdar M. 2002). There, NM II interacts with actin to form actomyosin networks that can produce contraction forces (Mazumdar A. and Mazumdar M. 2002).

The first phase of cellularization lasts around 10 minutes and proceeds with the invagination of cell membranes into the regions between the nuclei (Gilbert 2000, Mazumdar A. and Mazumdar M. 2002, Sokac et al. 2022). At the same time, the nuclei start to elongate. The second phase lasts around 20 minutes, during

which all the nuclei have completed their elongation. In phase 3 (~20 min), the furrow canals move inward at a slow rate until they reach the basal ends of the elongated nuclei. Each nucleus is surrounded by an actomyosin hexagonal structure that is connected to form a network over the embryo surface (Mazumdar A. and Mazumdar M. 2002). The hexagonal structure begins rounding up to form rings during phase 3 (Sokac et al. 2022). This is followed by phase 4 (~20 min), which is the late fast phase (Mazumdar A. and Mazumdar M. 2002). During this, the rate of inward movement of furrow canals increases significantly. The whole cellularization process takes around 60-70 minutes to complete (Gilbert 2000, Mazumdar A. and Mazumdar M. 2002, Sokac et al. 2022). During fast phase, formed rings begin gradually get smaller in diameter as the furrow canals reach their final length, after which they are pinched off to form the blastoderm cells (Mazumdar A. and Mazumdar M. 2002).

How all the signals and timings are initiated for the cellularization, are still largely unknown, but multiple genes are known to be expressed in a pulse and downregulated immediately afterward (Sokac et al. 2022). These genes are not known to function at other times of the *D. melanogaster* life cycle, but in the early embryo, they are part of signaling pathways linked with actin-membrane interactions and morphogenesis (Sokac et al. 2022). However, the complex processes involved in cellularization require highly coordinated signaling from multiple proteins, such as actin crosslinking proteins, motor proteins, and regulating kinases. These are discussed in more detail below.

1.2 Actin crosslinking protein Filamin and mechanosensing

One of several known mechanosensory signaling mechanisms is linked to actin filaments, myosin motors, and actin cross-linking proteins. Filamins are actin cross-linking proteins that can respond to mechanical forces.

Filamins are long V-shaped proteins, comprising of two monomer chains, with each chain containing three regions: head, backbone, and tail (Figure 1a) (Gorlin et al. 1990). In the N-terminus, the head region contains the actin-binding domain (ABD), followed by the backbone immunoglobulin (Ig) -like rod domains. Two flexible hinges separate the Ig-like rod domains into two, and the C-terminal (tail) functions as a dimerization site (Gorlin et al. 1990, Pudas et al. 2005).

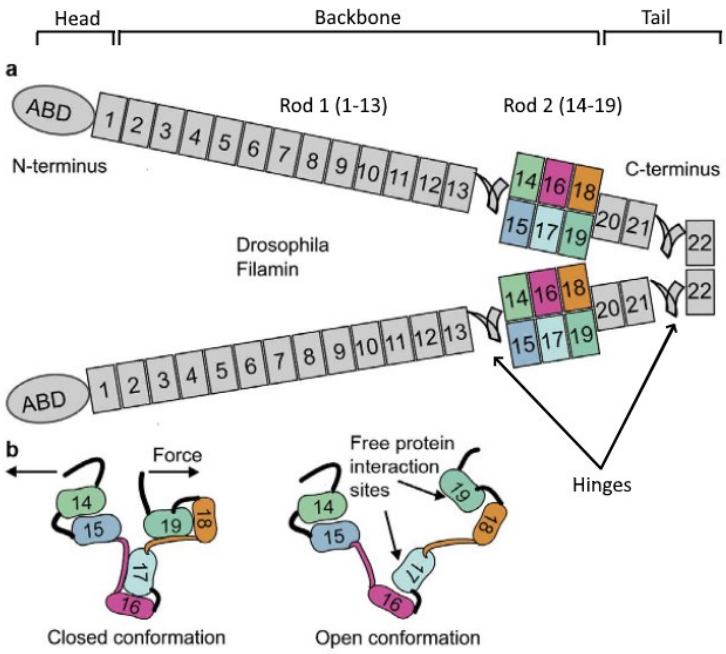

Figure 1. Structure of filamin. A schematic view of *Drosophila* filamin Cheerio: The filamins structure (a) consists of two homodimers, each containing an ABD domain in the N-terminus and two Ig-like rod domains separated by two flexible hinges. The C-terminus functions as a dimerization site. The rod 2 Ig-like domain contains mechanosensitive region (MSR) (b) that can change its conformation from closed to open when induced by force. The open conformation allows access to other protein interaction sites that can lead to other response mechanisms. Figure adapted from Huelsmann et al. 2016. CC BY 4.0.

The ABDs allow filamin to cross-link actin to form actin networks but also couple with a variety of other factors, such as intracellular signaling molecules, receptors, transcription factors, and cytoskeletal and adhesion proteins (Stossel et al. 2001, Popowicz et al. 2006, Zhou et al. 2007, Stossel et al. 2010, Nakamura et al. 2011, Razinia et al. 2012).

Filamins are linked to mechanical cell processes, such as cell motility and membrane stability, but also as a protective measure against tensile forces (Cunningham et al. 1992, Glogauer et al. 1998, D'Addario et al. 2001, D'Addario et al. 2002, Kainulainen et al. 2002, Gehler et al. 2009). In addition, they provide stability to cells by promoting actin filament recruitment. For example, under force, filamins accumulate actin filaments to the extracellular adhesion sites, providing stability for the plasma membrane (Glogauer et al. 1998). Furthermore, several studies show that filamins are central to other complex mechanical processes in cell development, such as cell differentiation and morphogenesis (Krakow et al. 2004, Lu et al. 2007, Bello et al. 2009).

Due to their importance in cellular processes, defective filamins can cause multiple disorders. Mutations in filamins that affect their functionality can cause myopathies (filaminopathy) in humans (Kley et al. 2012, Fürst et al. 2013). Several

known mutations can affect the functionality of the actin-binding domain, Ig-like rod domains, and the dimerization domain (Fürst et al. 2013).

Structural studies show that filamins contains mechanosensitive protein interaction sites (MSR) (Lad et al. 2007, Heikkinen et al. 2009) that can be exposed by force generated by myosin motors (Figure 1b) (Rognoni et al. 2012). These sites act as binding sites for several proteins, allowing diverse and flexible functionality for different cellular processes (Razinia et al. 2012). *Drosophila* orthologue Cheerio (Cher) has been identified and used for studies related to their role actin organization during development (Robinson et al. 1997, Li et al. 1999, Sokol & Cooley 1999). Filamin has a mechanosensitive function where the mechanical force opens its mechanosensitive binding sites essential for actin organization during *Drosophila* oogenesis (Huelsmann et al. 2016). Moreover, Cheerio is needed for proper development in early embryogenesis (Krueger et al. 2019).

1.3 Myosin II

Myosin's are molecular motors that bind to actin filaments and can convert ATP into mechanical force (Vicente-Manzanares et al. 2009). Most myosin belongs to class II, which forms most of the cardiac, skeletal, and smooth muscle contractile proteins together with actin. Similar myosin II molecules are found in all non-muscle eukaryotic cells (Vicente-Manzanares et al. 2009).

Myosin II molecule's structure is a hexamer α-helical coiled-coil dimer structure composed of three pairs of peptides (Figure 2) (Vicente-Manzaranes et al. 2009). The N-terminus consists of two globular head domains, two regulatory light chains, and two essential light chains. The essential light chains function as a stabilizing factor for the globular head domain structure, while the regulatory light chains regulate the activation of the myosin. The globular head domains consist heavily conserved of enzymatic Mg^{2+}-ATPase motor domains. These domains are also known as ABDs, as they can bind to actin filaments and drive the movement along actin filaments. The N-terminus domains are attached to the coiled-coil myosin heavy chain by the neck domain, enabling movement generation by the motor domain. The coiled-coil myosin heavy chains contain a non-helical tail at the C-terminus. Myosin II molecules have two conformations: the folded inactive 10S assembly-incompetent formation and the active unfolded 6S assembly-competent form. The transformation between inactive and active conformations is regulated by regulatory light chain phosphorylation (Vicente-Manzanares et al. 2009).

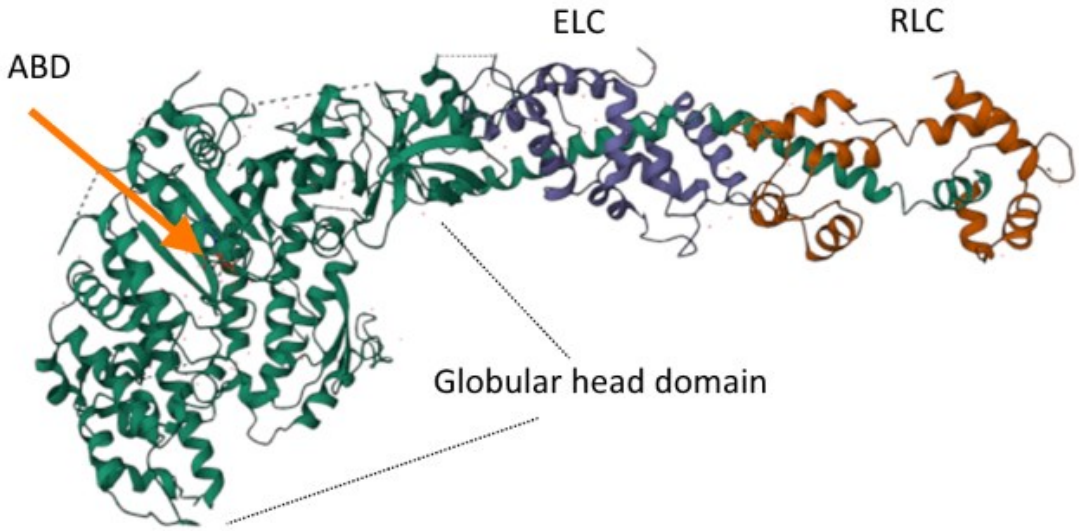

Figure 2. A novel structure of the myosin head. Image shows part of the myosin structure of the N-terminal, where we can see the globular head domain with actin binding site (ABD) (green), essential light chain (ELC) (blue) and the regulatory light chain (RLC) (orange). These structures are attached to the coiled-coil heavy chain (not shown). PDB ID: 1B7T (Houdusse et al. 1999).

Myosin II is a common force generator that drives several different cellular changes (Vicente-Manzanares et al. 2009). Myosin II has fundamental role in multiple cellular and developmental processes, such as cell adhesion (Conti et al. 2004, Shewan et al. 2005), cell migration (Betabudi et al. 2006), regulation of stiffness and stress (Singh et al. 2021), and cytokinesis (Ma et al. 2012), in both muscle and non-muscle cells. Regulatory light chain activity is controlled by different kinases and phosphatases that act as downstream components of several signal transduction pathways (e.g., mechanotransduction) (Heissler and Sellers 2014). In addition, phosphorylation of regulatory light chain also regulates myosin motor activity (Heissler and Sellers 2014).

Regulation of actomyosin networks is crucial in normal development (Chougule et al. 2016). However, many aspects of the cellular processes are still not fully understood. Nevertheless, non-muscle myosin II (NM II) light and heavy chain phosphorylation is central in actin-myosin contractile system regulation (Vicente-Manzanares et al. 2009). Furthermore, NM II is involved in cell force generation and response mechanisms (Shutova and Svitkina 2018). These responses have been studied in *D. melanogaster* during early embryonic development (Vicente-Manzanares et al. 2009). In *Drosophila*, NM II heavy chain is encoded by gene *zipper* (Young et al. 1993) and the regulatory light chains are encoded by *spaghetti squash* (Sqh) (Karess et al. 1991, Pascale and Karess 1997). Regulatory light chains contain conserved serine/threonine sites that are phosphorylated to activate the NM II (Vicente-Manzanares et al. 2009, Heissler and Sellers 2014, Vasques et al. 2016). The regulatory light chains' Ser19 and

Thr18 are highly conserved regions that can be phosphorylated by multiple kinases and phosphates (Vicente-Manzanares et al. 2009). These include but are not restricted to myosin light chain kinase MLCK, Ca^{2+}/calmodulin-dependent kinases, such as ROCK and DAPK (Rok & Drak in *Drosophila*), Rho GTPase, and leucine zipper interacting kinase (ZIPK/DAPK3) (Murata-Hori 1999, Kuo et al. 2003, Dean and Spudich 2006, Ueda et al. 2006, Neubueser and Hipfner 2010). They play a crucial role in tightly controlling the levels of phosphorylation of regulatory light chain (Heissler and Sellers 2014). Although these kinases phosphorylate the same site in regulatory light chains, the activating signals for these kinases differ. For example, some kinases target only NM II, such as MLCK, but others, such as ROCK, can have multiple substrate targets (Vicente-Manzanares et al. 2009). Furthermore, these conserved sites can be either mono- or di-phosphorylated by phosphorylating only Ser19 or by both Ser19 and Thr18 sites (Vicente-Manzanares and Horwitz 2010). The different effects of mono- or di-phosphorylation has not been widely studied, however, mono-phosphorylation is known to promote adhesion maturation within protrusions and generate focal adhesion throughout the cell. Di-phosphorylation on the other hand induces localized large adhesions and actomyosin bundles in distinct cell regions (Vicente-Manzanares and Horwitz 2010).

NM II regulation have been studied with *Drosophila* embryo cellularization. For example, Crawford et al. (1998) demonstrated that Rho subfamily of Ras-related G proteins (Rho and Cdc42) affect the formation of actomyosin cytoskeleton. They guide nuclei to their correct locations and ensure proper formation of actomyosin-driven furrow canals. During *D. melanogaster* cellularization, defects in Rho and Cdc42 proteins cause nuclei aggregation and hexagonal array disorganization due to actin disruption. This disrupts the cellularization process and stops it from proceeding to gastrulation. Furthermore, inhibition of Rho halts the progression of the cellularization by preventing activation of myosin required for the force production of cytokinesis (Crawford et al. 1998). Thus, it is suggested that the Rho GTPase acts as an upstream regulator for MLCK-kinases and phosphorylation of NM II. Furthermore, the geometrical organization of actin filaments affects contractility (Krueger et al. 2019). During early cellularization, hexagonally arrayed actomyosin fibers resists myosin II activation. However, when the actomyosin fibers arrange to ring-like conformation, it becomes sensitive to myosin II. Actomyosin hexagonal patterning is regulated by short expression of the protein bottleneck and controlled by two actin cross-linking proteins, filamin and fimbrin (Krueger et al. 2019).

1.4 *Drosophila* cellularization is dependent on Drak

In *Drosophila,* two potential candidates, RhoGTPase effector ROCK (Rok in *Drosophila*) and Drak, have recently been proposed as regulators of NM II phosphorylation during cellularization *in vivo* (Neubueser and Hipfner 2010). The pairwise sequence analysis shows that Drak is most similar to DRAK1, with

50% of their sequences being identical and 72% similarity with the kinase domain in the N-terminal. However, the C-terminal tail of Drak is non-conserved, longer, and does not contain any recognizable domains (Neubueser and Hipfner 2010).

Neubueser and Hipfner (2010) study established that lack of Drak leads to defects in epithelial tissues. Drak and Rok have overlapping roles in epithelial morphogenesis and Drak is only essential when Rok levels are reduced. Similarly, as Rok, Drak regulates NM II by phosphorylating Sqh. Additionally, Drak and Rok also co-regulate adherent junction remodeling during eye development (Robertson et al. 2012).

Proper formation of the actomyosin networks during development in *Drosophila* depends on the presence of Drak (Chougule et al. 2016). Their study tested viable mutant flies with a complete deletion of Drak ($Drak^{del}$) and a deletion of the domain of Drak ($Drak^{ko}$).

$Drak^{del}$ mutant embryo affects mono- and di-phosphorylation (Ser21 & Ser21/Thr20) levels of Sph (Chougule et al. 2016). The levels of mono-phosphorylation of Sqh were reduced by 94 % during early cellularization and by 84 % during late cellularization. Additionally, Sqh mono-phosphorylation is heavily reduced before cellularization and during gastrulation but not as severely. Expression of phosphorylated Sqh completely rescues NM II organization and function in $Drak^{del}$ mutants, confirming Drak's central role in Sqh phosphorylation. Furthermore, Drak mutants lead to a wavy actin front due to the abnormal microfilament ring shapes (Chougule et al. 2016). When actin front passes the nuclei, the NM II shows organization defects in areas with reduced NM II. However, these defects show less severity compared to early cellularization. In addition, NM II becomes clustered and scattered between regions rather than being evenly distributed. This indicates that Drak is necessary for arranging NM II into contractile rings. Defective Drak also affects actomyosin network constriction during the early and late phases of cellularization (Chougule et al. 2016). During late phases, the actin front shows reduced constriction, suggesting defective but not entirely lost actomyosin constriction. These results imply that Drak is also needed for actomyosin contraction during cellularization, but other kinases might work synergistically. Moreover, Drak is central in the formation of correct furrow canal structure and plasma membrane integrity (Chougule et al. 2016). In the $Drak^{del}$ mutant, the structure of the furrow canal is narrow at the bases and appears collapsed compared to the teardrop-shaped furrow canals in wild-type (WT). In late phases of cellularization, $Drak^{del}$ furrow canals show noticeable membrane blebbing in many regions of the lateral plasma membrane compared to the WT embryo. This would suggest a loss of integrity of the furrow membrane or the cortical cytoskeleton (Chougule et al. 2016).

The study findings by Chougule et al. (2016) suggest that Drak is a central MLCK-like protein kinase that phosphorylates Sqh and is required for the organization of NM II within the microfilament ring. Additionally, Drak seems to be responsible for the maintenance of furrow canal structure and plasma membrane integrity, which suggests that Drak might be the main regulator of

actomyosin dynamics in the early development of *Drosophila* (Chougule et al. 2016).

Ylänne J. (unpublished) yeast two hybrid (Y2H) study with Cher MSR^{open} showed potential interaction with Drak homolog of DAPK family member. The analysis located the potential interaction site of Cher to the nonconserved C-terminal side of Drak (Ylänne J. unpublished). Furthermore, Koskela I. study (unpublished) biochemically confirmed the interaction between the C-terminal end of Ser/Thr kinase Drak and the MSR of *Drosophila* filamin Cher. Drak exhibits a stronger binding affinity for the Cher MSR^{open} mutant compared to the Cher MSR^{closed} variant. This indicates that Drak binds to the Cher Ig-like domain when the MSR binding sites are accessible (Koskela I. unpublished). These results suggest that the Drak-Cher binding interaction requires opening of the MSR and play a role in mechanotransduction pathways.

In summary, the loss of function of Drak causes defective formation during embryogenesis, which would suggest that its function is central to tissue development. The hypothesis of this study was that if Drak is the main MLCK that regulates phosphorylation of the regulatory light chain during cellularization, it will colocalize with Cher in the actin front. It would support previous findings that Drak can bind to the Cher mechanosensitive region. The aim of this thesis was to examine the Drak localization during *D. melanogaster* cellularization. This was studied by time-lapse live-imaging confocal microscopy of fluorescence tagged Drak, Sqh, and Cher expressing embryos. These results would further our knowledge about the mechanotransduction signaling pathways.

2 MATERIALS AND METHODS

2.1 *Drosophila* stocks

In this experiment, embryos from four different fly lines were used (Table 1).

TABLE 1. Used fly lines and their genotype.

Fly lines:	Genotype:
Cher-mCherry	w;; P{ry[+t7.2]=neoFRT}82B GT{GMR-w[+]=cher[mCherry-2]}/ TM6B, P{Dfd-GMR-nvYFP}4, Hu, Sb[1] Tb[1] ca[1]
Drak-GFP	*y[1] sc[1] v[1] Drak[GFP-*3xP3DsRed];;Pri/TM6(Hu)
Sqh-mCherry;Cher-GFP	Cher-GFP: w; P[w+, Sqh::mCherry]/CyO; P{ry[+t7.2]=neoFRT}82B GT{GMR-w[+]=cher[mCherry-2]
Drak-GFP;Cher-mCherry	*y[1] sc[1] v[1] Drak[GFP-*3xP3DsRed];; P{ry[+t7.2]=neoFRT}82B GT{GMR-w[+]=cher[mCherry-2]}

Cher-mCherry fly line was created by Huelsmann S. and Ylänne J. (unpublished), which was generated as described in Huelsman et al. (2016).

Drak-GFP was generated by CRISP method using pScarlessHD-DraksfGFP-3xP3DsRed plasmid as a homologous recombination donor (Green H. and Ylänne J. unpublished). pScarlessHD-sfGFP-3xP3DsRed was a gift from Kate O'Connor-Giles (Addgene plasmid # 80811). Sqh-mCherry;Cher-GFP was generated by crossing w[*]; P[w+, Sqh::mCherry]/CyO; Sb/TM3, Ser (Izquierdo et al. 2018) with the Cher-GFP fly line. Drak-GFP;Cher-mCherry was generated by crossing the Drak-GFP and Cher-mCherry stock.

2.2 Sample preparations

Flies were kept in a cultivation vial that contain Nutri-Fly Bloomington Formulation (Genesee Scientific) with added propionic acid. Cultivation vials were kept at 25 °C with 12 h light and 12 h dark cycle.

Newly hatched flies were used in the experiment and transferred to the cage with embryo collection 60x15 mm agar plate (Sartedt, Tissue Culture Dish) containing FlyStuff Grape Agar Premix at the bottom. A droplet of fresh yeast was added to the agar plate to increase the mating and egg laying to the dish. After two to three hours plates were collected and replaced.

The collected agar plate was covered with 100% halocarbon oil (Sigma-Aldrich) to make them more transparent to the light microscopy. For the live-imaging embryos, that were in their early stage before cellularization had started, were collected. For fixed images, embryos in the process of cellularization, were collected. By carefully moving the embryos with tweezers, they were clumped together in the collecting agar plate and then transferred to a new empty plate containing a piece of dry tissue paper to dry any excess oil. After drying, the embryos were transferred to a paper coated with 5 % Na-hypochlorite for 30-45 seconds in order to dechroniate them. The embryos were exposed to the Na-hypochlorite by gently swirling them over the paper.

Embryos were then transferred between three to four distilled water droplets to remove traces of hypochlorite. After rinse, a piece of dry tissue paper was used to remove any remaining water droplets from the embryos. Subsequently, using tweezers or a modified small pipette tip, the dried embryos were gently transferred into the cell imaging dish (IBIDI®, µ-Dish 35 mm, high Glass Bottom). Care was taken to position the embryos in a dorsolateral orientation within the dish, avoiding overlapping.

For live-imaging, the embryos were covered with phosphate-buffered saline (PBS) containing 1.0 µM of ascorbic acid as an antioxidant to reduce phototoxicity (Harada et al. 2022). The PBS contained 137 mM NaCl, 27 mM KCl, 2 mM KH_2PO_4, 8 mM Na_2HOI_4 and a pH of 7.4). Fixed samples were treated 15 minutes with 8 % paraformaldehyde (PFA, pH 7.0, stored in -20°C freezer) diluted to 4 % PBS. PFA was added to the embryos after they were transferred to the imaging disc. After fifteen minutes, embryos were washed with PBS three times.

2.3 Confocal microscopy

For imaging, high-speed Leica TCS SP8 Falcon (FAst Lifetime CONtrast) confocal microscopy was used. For the excitation of GFP- and mCherry-tagged proteins, 488 nm and 583 nm were used, with a detection range 8 nm or higher from the excitation range to avoid unwanted signals. Images were captured with the Leica Lightning / Thunder processing, in which we were able to use the deconvolution processing that calculated the Point Spread Function (PSF) correction automatically. The PSF refraction index was set to 1.33 with other settings as default. Deconvolution was used to reduce the noise from the images and increase the visibility of low signal from the background. Validation of the deconvolution results is presented in the Appendix 1 and 2.

Resolution was set to 248 x 248 (14.19 x 14.19 µm) (voxel size 0.057 µm) and Z-stack size set to ~20 µm with optimum voxel size. Microscopy numerical aperture (NA) was set to 1.2. Images were taken with 1.1 AU pinhole with zoom set to 13.00, 760 Hz Scan Speed, and Line Average set to 2. Image stacks were imaged with 5-minute time interval until actin front was not visible. White light laser (WLL) output power was 70 %. Images were captured with sequential imaging where sequential intensity setting for the 1st was set to the laser line (488 nm) to 10 % and laser line 2 (588 nm) to 0%. For the 2nd sequential setting, the 488 nm was set to 0 % and the 588 nm to 2 %. Detectors used for the lasers were Leica's hybrid photodetector (HyD) for single molecule detection (SMD) 495-525 nm and HyD SMD for 595-650 nm. These detectors were chosen as they allow observation of fast cellular processes while providing high dynamic range and contrast (Leica Microsystems). Both detectors gain was set to 500.

2.4 Image analysis and colocalization

Statistical analyses were tested with IBM SPSS (20.0.0) and images were analyzed with FIJI ImageJ 1.8.0 image processing software version 1.53k (Schindelin et al. 2012). Visual qualitative analysis of images was conducted by superimposing images. Quantitative analysis colocalization was done by measuring Pearson's Correlation Coefficient (PCC) and Manders' Colocalization Coefficient (MCC) from the images. For PCC analysis, randomized data was generated with Costes' randomization for the Drak-GFP;Cher-mCherry fly line.

Actin front was detected and measured with the help of Z-axis profile that shows the mean intensity on the Y-axis and Z-stack as an X-axis. Three 124x124 mm regions-of-interests were selected from each timepoint from the Z-direction (top view) and the XZ-direction (cross-section view). Z-stack size was determined from the actin front intensity profile for each timepoint (marked with half bracket in images merge channel). After this, both (top view and cross-section) was processed with summarized Z-projection. Images were converted to 8-bit to scale the bit depth to 0-255 bits per pixel. The colocalization calculations

were restricted to these projections. For mean intensity plots, signal intensity was measured from both channels and normalized to fit.

Colocalization was measured with JACoP plugin. The top view and cross-section view were averaged for each regions-of-interest to take both dimensions into account. MCC were measured from the same images as control Drak-GFP, and both Cher-GFP;Sqh-mCherry and Drak-GFP;Cher-mCherry to see if the results align with the PCC measurements. Colocalization changes during cellularization progression were investigated by measuring the actin front distance from the embryo cortex. This was done by measuring the distance from the peak of the signals originating from the actin front to the signal peak originating from the cortex. Measured PCC values from Cher-GFP;Sqh-mCherry and Drak-GFP;Cher-mCherry were then plotted to the actin front distance.

The effect of noise to the PCC analysis was estimated by taking two consecutively image stacks and measuring the PCC values by comparing the same channels from different timepoints, T1 and T2, to each other. From that, replicate-based noise corrected correlation (RBNCC) was calculated using the Correction Factor (C_{gr}) (Adler et al. 2008) (1). Correction Factor C_{gr} was then applied to the measured mean colocalization (r_{mrg}) to get the corrected colocalization (r_c) (2).

$$C_{gr} = \frac{1}{\sqrt{r_{gg} \times r_{rr}}} \tag{1}$$

Where C_{gr} is the Correction Factor; r_{gg} is the measured PCC value of the T1 and T2 from the green channel and r_{rr} is the PCC value of the T1 and T2 of the red channel.

$$r_c = r_{mrg} \times C_{gr} \tag{2}$$

Where r_c is the corrected colocalization and r_{mrg} is the measured mean colocalization between fluorophores. The r_{mrg} consists of calculated mean from four green-red estimations of the measured colocalization ($r_{g1r1}, r_{g1r2}, r_{g2r1}, r_{g2r2}$). This was calculated for both top and cross-section views, which were then averaged.

2.5 Statistical analysis

Pearson's Correlation Coefficient (PCC) was measured from all embryos and randomized data generated by Costes' randomization (Appendix 4). For the independent t-test, a two-tailed analysis with a 95 % confidence level was selected, considering the PCC values ranged between [-1.00, 1.00], including both negative and positive values.

All groups underwent Kolmogorov-Smirnov and Shapiro-Wilkins normality testing at a 95 % confidence level (Appendix 5). The Levene's test for equality of variances was performed across all fly lines (Appendix 6). Due to unequal variances and non-normal distributions between some groups, I used bootstrap (sample size 1000) bias-corrected accelerated interval (BCa) method to correct for bias and skewness in the distribution of bootstrap estimates (Appendix 6).

3 RESULTS

In the results section I will show the results of time-lapse images of Drak-GFP;Cher-mCherry and Cher-GPF;Sqh-mCherry and their colocalization. Analysis of PCC and MCC is also reported. All the images were processed with deconvolution, which reduced noise and improved image quality (Appendix 1) but also the PCC analysis (Appendix 2).

3.1 Time-lapse images show Drak-GFP localization during cellularization

Drak-GFP localization and progression during cellularization was studied by taking time-lapse images from Drak-GFP;Cher-mCherry expressing embryos. The cross-section images contains the whole Z-stack (20 μm), while the top view has been selected just from the actin front for clarity (marked by half bracket in the merged images). Mean intensity plots were then produced from the the corresponding images.

In y-z projected images, Drak-GFP was initially mainly cytoplasmic above the nuclear layer near the cortex, indicated by yellow arrows (Figure 3, time point 1). As the Cher-mCherry position in the actin front layer progressed, an increase of Drak-GFP signal was seen between the nuclei, indicated by white arrows (Figure 3, time point 2-6). The progression of this signal followed the Cher-mCherry signal (Figure 3, merged time point 2-7). There appeared to be a limited increase in signal intensity in the Drak-GFP channel. Furthermore, there were no observation of detectable color hue changes in the merged panels, suggesting that the Drak-GFP signal remained relatively consistent throughout the progression of the cellularization. However, this observation may be more challenging to detect visually due to the relatively low signal level of Drak-GFP.

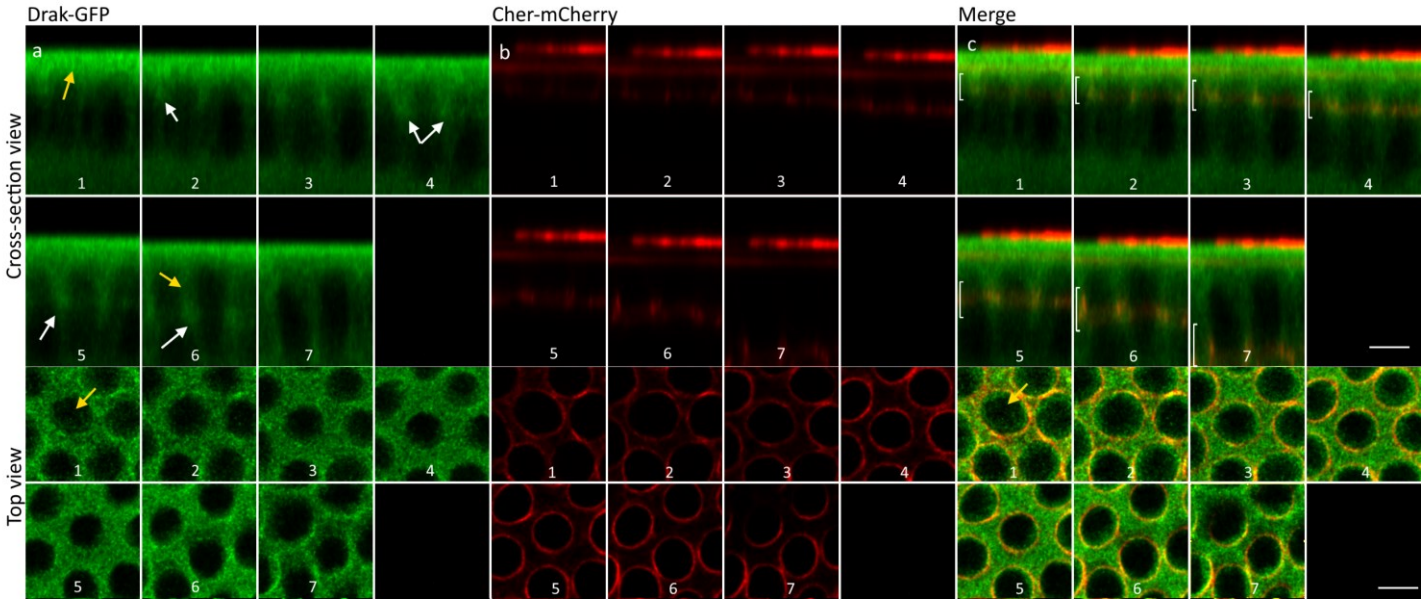

Figure 3. Timelapse images from Drak-GFP;Cher-mCherry. On the left (a) Drak-GFP channel where top panel contains the cross-section view and below the top view. In the middle (b) Cher-mCherry channel and the third panel (c) merged image of the two channels. White bracket in the merge channel indicates the Z-projection corresponding to top view images. Time between the images (1-7) was 5 minutes. Scale bar was set to 5 μm.

In the normalized mean intensity plots, a high peak of Drak-GFP was observed near the cortex throughout the cellularization process (Figure 4). However, along the z-axis, the Drak-GFP cytosolic peak followed the Cher-mCherry intensity peak in the actin front (Figure 4). The Drak-GFP signal peaks gradually became more noticeably and align with Cher-mCherry peak signals. Compared to Cher-mCherry signal, Drak-GFP did not exhibit distinct high peaks in the actin front, suggesting a weaker fluorescence signal. It is possible that the presence of surrounding signal in the cytosol obscured the already weak Drak-GFP signal in the actin front. In line with the images (Figure 3), the Drak-GFP signal intensity displayed minimal increase during the actin front progression (Figure 4).

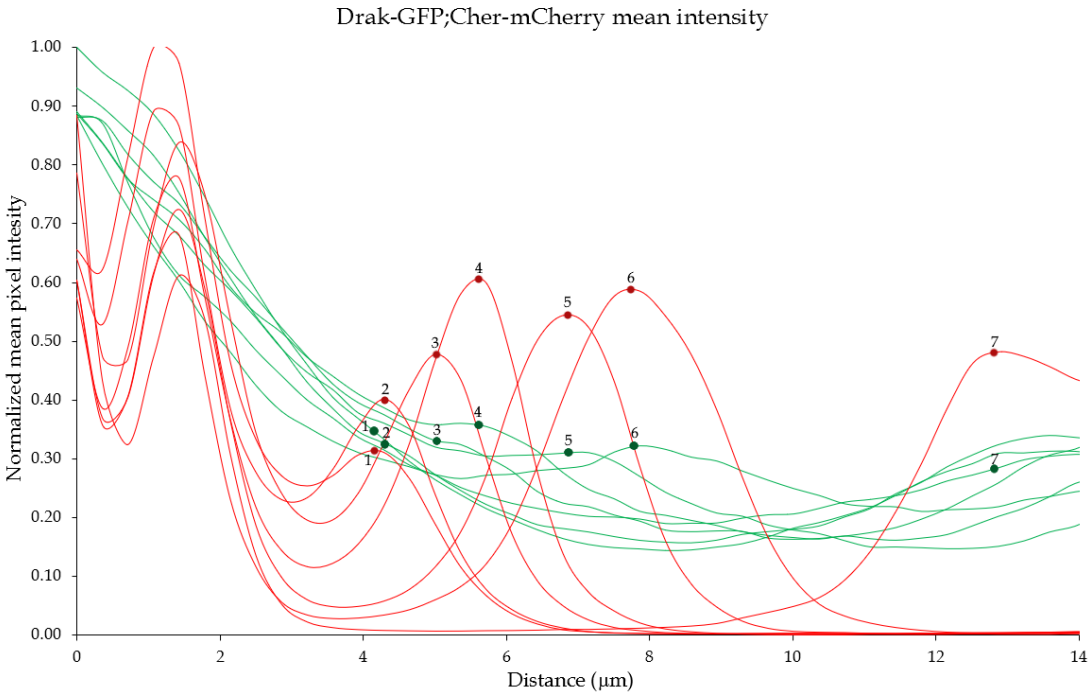

Figure 4. Drak-GFP;Cher-mCherry normalized mean intensity from different timepoints. Plot shows the normalized mean intensity changes from different timepoints (1-7) that were presented in the Figure 3. Green lines represent the green channel (Drak-GFP) and the red lines the red channel (Cher-mCherry). X-axis is the Z-stack 0-14 µm represented here as a distance from the cortex and y-axis the normalized mean pixel intensity. Image was Z-shift corrected by using peak autofluorescence signal emitting from the cortex in the red channel.

To make sure that the advancing Drak-GFP signal was not carryover from Cher-mCherry channel, time-lapses from Drak-GFP and Cher-mCherry was captured separately (Appendix 3). These results show that the Drak-GFP signal was validated.

A positive control Cher-GFP;Sqh-mCherry expressing embryos was similarly imaged (Figure 5). Here, Cher fluorescence was on similar depth as Sqh-mCherry, but the x-y projection of Cher-GFP was more confined than Sqh-mCherry (Figure 5). Compared to Cher-GFP, Sqh-mCherry channel exhibited fluorescence signal originating from both the embryo cortex and cytosol (yellow arrows). However, Cher-GFP signal was also present in the cytosol in addition to the actin front. When assessing the cross-section and top views, it was evident that the Cher-GFP signal initially presented higher intensity compared to Sqh-mCherry, as exemplified in time points 1-4 (white arrows). In image time points 1, 2, and 7, the top view revealed that the Cher-GFP signal was initially evenly

distributed but quickly became more concentrated in areas surrounding the nuclei (cyan arrows).

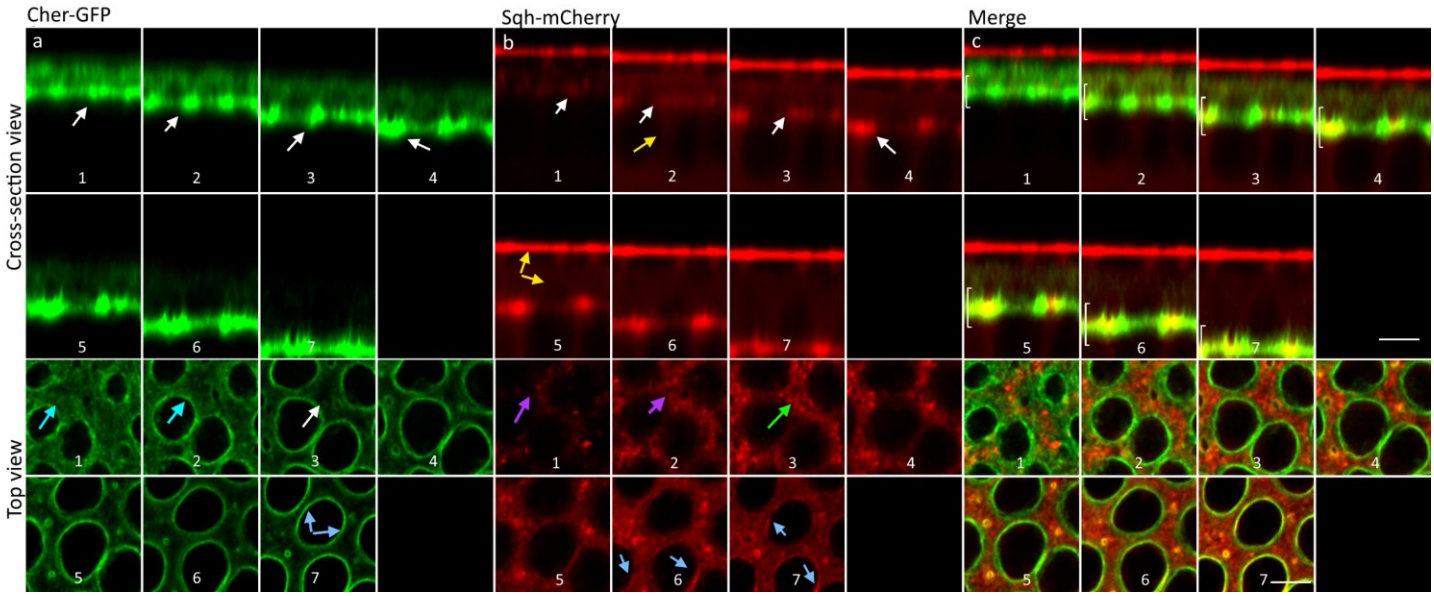

Figure 5. Timelapse images from Cher-GFP;Sqh-mCherry. On the left (a) Cher-GFP channel where top panel contains the cross-section view and below the top view. In the middle (b) Sqh-mCherry channel and the third panel (c) merged image of the two channels. White bracket in the merge channel indicates the Z-projection corresponding to top view images. Time between the images (1-7) was 5 minutes. Scale bar was set to 5 µm.

Observations in Sqh-mCherry channel was a bit different. Contrary to the Cher-GFP, the Sqh-mCherry signal was initially relatively low (time point 1-2) and more concentrated at areas between the nuclei (purple arrows). As the cellularization progressed (time point 3) the Sqh-mCherry signal increased and became more dispersed throughout the actin front (green arrow). However, if we look at top view of time point 3, for example, compared to the Cher-GFP, the signal was not concentrated at the edges surrounding the nuclei. As the cellularization progressed further, this signal became more evenly distributed throughout the structure. Towards the late phases (time points 6-7), the signal increases more on the edges surrounding nuclei, similarly to the Cher-GFP (blue arrows). Colocalization was observed in the merge panels, where there was a subtle change in the color hue from green to yellow as the Sqh-mCherry activity increased.

The normalized mean peak signals originated from the same distance, suggesting that Cher-GFP and Sqh-mCherry are localized to the actin front and comigrate (Figure 6). Specifically, the Sqh-mCherry signal displayed lower intensity at the initial stages of the cellularization (time points 1-4). As the cellularization advanced (time points 5-7), the Sqh-mCherry signal showed a noticeable increase in intensity. Moreover, it is noteworthy that the Cher-GFP signal also exhibited some increase in intensity as the cellularization progressed;

however, this increase was not as pronounced as Sqh-mCherry. These results coincide with the observation in the images (Figure 5).

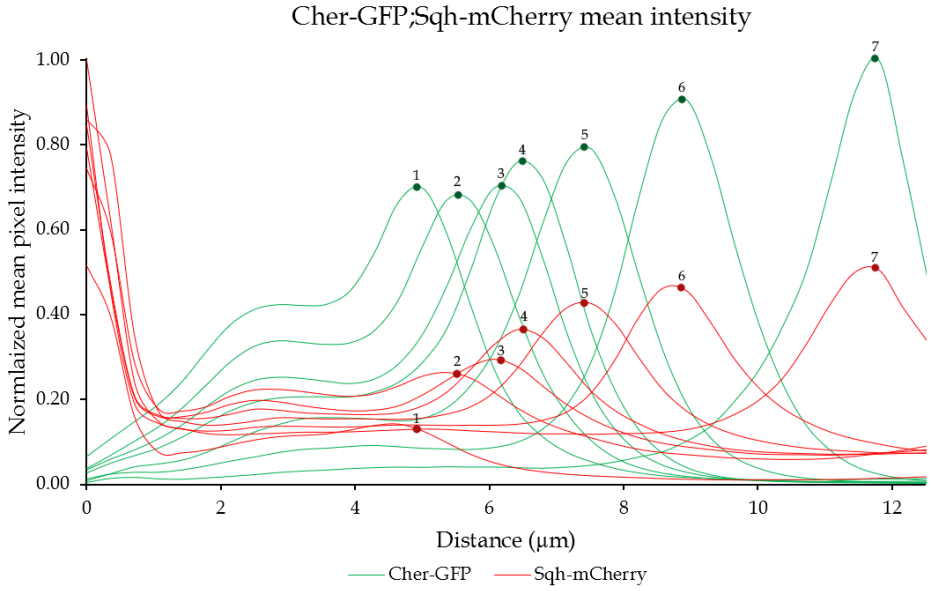

Figure 6. Cher-GFP;Sqh-mCherry normalized mean intensity from different timepoints. In this image we can see the normalized mean intensity changes from different timepoints (1-7) that were shown in the Figure 5. Green lines represent the green channel (Cher-GFP) and the red lines the red channel (Sqh-mCherry). X-axis is the Z-stack 0-13 µm represented here as a distance from the cortex, and y-axis the normalized mean pixel intensity. Image was Z-shift corrected by using peak autofluorescence signal emitting from the cortex in the red channel.

These results show that Drak-GFP localizes to the actin front and comigrates with Cher-mCherry during cellularization. The image results also show that the Cher localizes more around the nuclei, while Sqh is more dispersed on the actin front. However, as the cellularization progresses, the signal becomes more evenly distributed and shows localization around the nuclei. Furthermore, the Sqh signal increases quite significantly as the cellularization progresses. A similar concentration and increase of Drak-GFP signal are not observed. Furthermore, compared to the positive control, Drak-GFP colocalization with Cher-mCherry does not seem to be as strong due to a weak Drak-GFP signal.

3.2 Drak localization changes in the cell cortex prior cellularization

One of the unexpected results from this study was that Drak-GFP signal was high prior to the cellularization phase. Drak-GFP signal was found to be elevated near the cortex during the last nuclei divisions and formation of new furrow canals (Figure 7). Furthermore, before the actual early actin front formation and progression, Drak-GFP signal was also elevated in the furrow canals in a supposed priming phase.

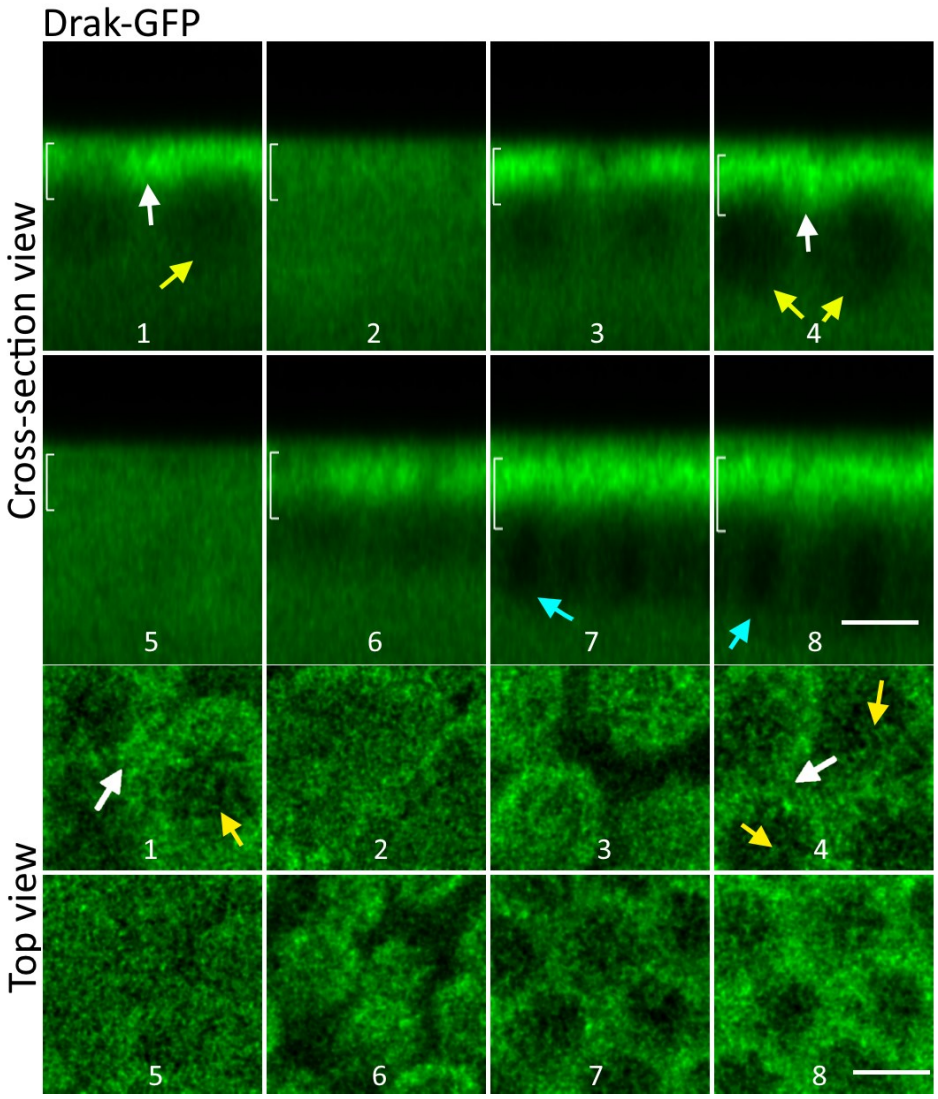

Figure 7. Drak-GFP signal during nuclei divisions and priming phase. Images were taken from Drak-GFP control embryos. On top, the cross-section view of the Z-stack and on the bottom panel the top view from Z-stacks taken near the embryo cortex marked by half bracket. Time between the images (1-8) was 5 minutes. Scale bar was set to 5 µm.

Presence of distinct signals during the last nuclei divisions is observed in Figure 7 time points 1-6. Time points 1, 3, and 4 notably showcased the roundness of the nuclei (yellow arrows) indicating early stages of development. Concurrently, during these phases, the Drak-GFP signal showed higher intensity in comparison to the background signal in the cytosol. This is seen when new membrane is formed between the new daughter cells, Drak-GFP signal is between the nuclei structures (white arrows). Furthermore, the signal is near the cell cortex and seems to be temporarily located on top of the nuclei (time points 3 and 6). During nuclei divisions, (time points 2 and 5), Drak-GFP signal diffuses to the cytosol, as there are no nuclear envelopes during mitosis. The beginning of

the cellularization slow phase can be seen time points 7 and 8, where the nuclei start their elongation process (cyan arrows).

3.3 Colocalization statistical analysis

To measure the degree of colocalization between Drak-GFP and Cher-mCherry, Pearson's Correlation Coefficient (PCC) was measured and compared to controls. Descriptive statistics of the measured PCC from the different embryos are detailed in Appendix 4. Potential differences in mean PCC values between groups were tested with Student's independent two-tailed t-test. Firstly, Kolmogorov-Smirnov and Shapiro-Wilkins were used to test the normal distribution of all groups (Appendix 5). As Levene's test showed unequal variances between some groups (Appendix 6), Welch's independent t-test was used instead. As Drak-GFP;Cher-mCherry and Cher-GFP;Sqh-mCherry did not show normal distribution due to skewness, Welch's independent two-tailed t-test was conducted also with bootstrap (sample size 1000) with bias-corrected accelerated interval (BCa). The reported p-values below are based on the results from the bootstrap method. The limit of statistical significance was $p \leq 0.05$ in all tests.

The mean PCC values between controls Cher-mCherry (0.25 ± 0.13) and Drak-GFP (0.26 ± 0.12) were compared (Figure 8). The analysis showed that the difference between control groups was not statistically significant ($p = 0.487$). Therefore, no substantial difference was observed between these two control groups. When control fly line Cher-mCherry PCC values were compared between Cher-GFP;Sqh-mCherry (0.66 ± 0.14), the analysis demonstrated a statistically significant difference ($p = 0.001$***). Similarly, a statistically significant difference was seen when control Cher-GFP was compared with fly line Drak-GFP;Cher-mCherry (0.56 ± 0.09). Both findings show that there are differences in PCC value between fly lines and negative controls containing only one fluorophore.

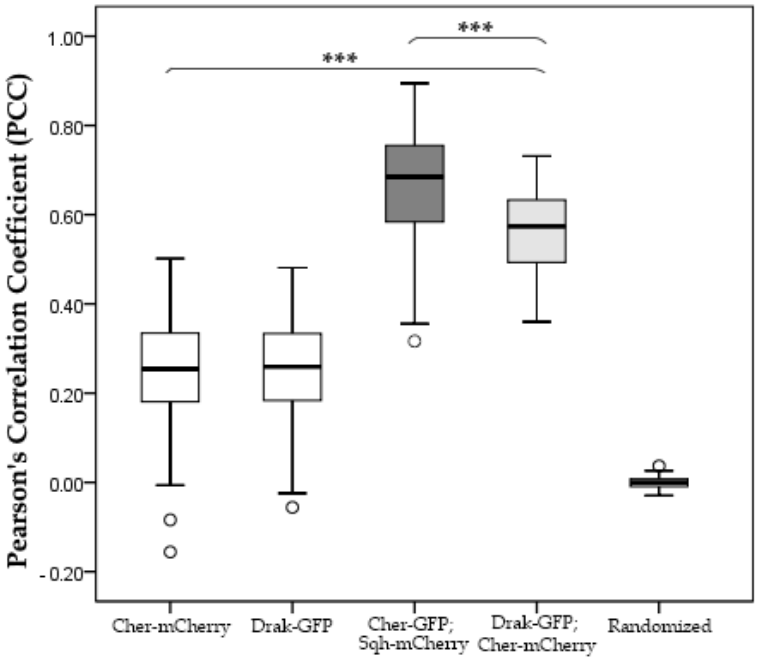

Figure 8. Pearson's Correlation Coefficient (PCC) measurements from two channels: X-axis shows the different fly line groups and y-axis shows the PCC value (-1.00 – 1.00). Control groups consisted of one fluorophore Cher-mCherry or Drak-GFP. Randomized group consisted of measurements of random white noise generated by Costes' randomization that was then superimposed to Drak-GFP;Cher-mCherry fly line Drak-GFP channel.

The Cher-GFP;Sqh-mCherry had a higher mean PCC value in comparison to Drak-GFP;Cher-mCherry, with a mean difference of approximately 0.10 (Figure 8). Statistical analysis further confirmed the presence of a statistically significant difference between these groups, thereby indicating a higher colocalization degree between Cher-GFP and Sqh-mCherry when contrasted with Drak-GFP and Cher-mCherry. Moreover, Drak-GFP;Cher-mCherry was subjected to comparison with randomized data (0.00 ± 0.01) generated using the Costes' randomization. The results disclosed a statistically significant difference ($p = 0.001$***) between the groups, providing evidence that the PCC values in Drak-GFP;Cher-mCherry are not attributable to random chance.

3.4 Effect of image noise on PCC, assessed with replicate-based noise analysis

To evaluate how much noise had an effect on PCC analysis, replicate-based noise analysis (RBNCC) test was conducted on fixed embryos from Drak-GFP;Cher-mCherry and Cher-GFP;Sqh-mCherry. This estimation was achieved by measuring PCC values from two separate image stacks obtained at consecutive timepoints (e.g., green channel T1 to green channel T2). The underlying theory is that the PCC values between T1 and T2 should be at 1.0 if noise has no effect, with scatterplot displaying perfect linear correlation. Subsequently, from these

different timepoints, the Correction Factor was calculated (1), a parameter used in estimating corrected PCC (2) values based in the RBNCC method (Adler et al. 2008). This analysis was applied to both Drak-GFP;Cher-mCherry and Cher-GFP;Sqh-mCherry fixed fly lines, with deconvolution processing techniques implemented similar to the time-lapse images.

Examination of Drak-GFP;Cher-mCherry (Figure 7) revealed presence of noise signal in the cytosol within the green channel associated with the Drak-GFP. The scatterplot pixels observed in the Drak-GFP channel were more widely scattered, resulting in PCC values deviating from the expected value (1.0). This deviation was more pronounced in the Drak-GFP channel compared to the Cher-mCherry channel. Both top view and cross-section view of the Drak-GFP channel PCC values were lower than those observed in the Cher-mCherry channel.

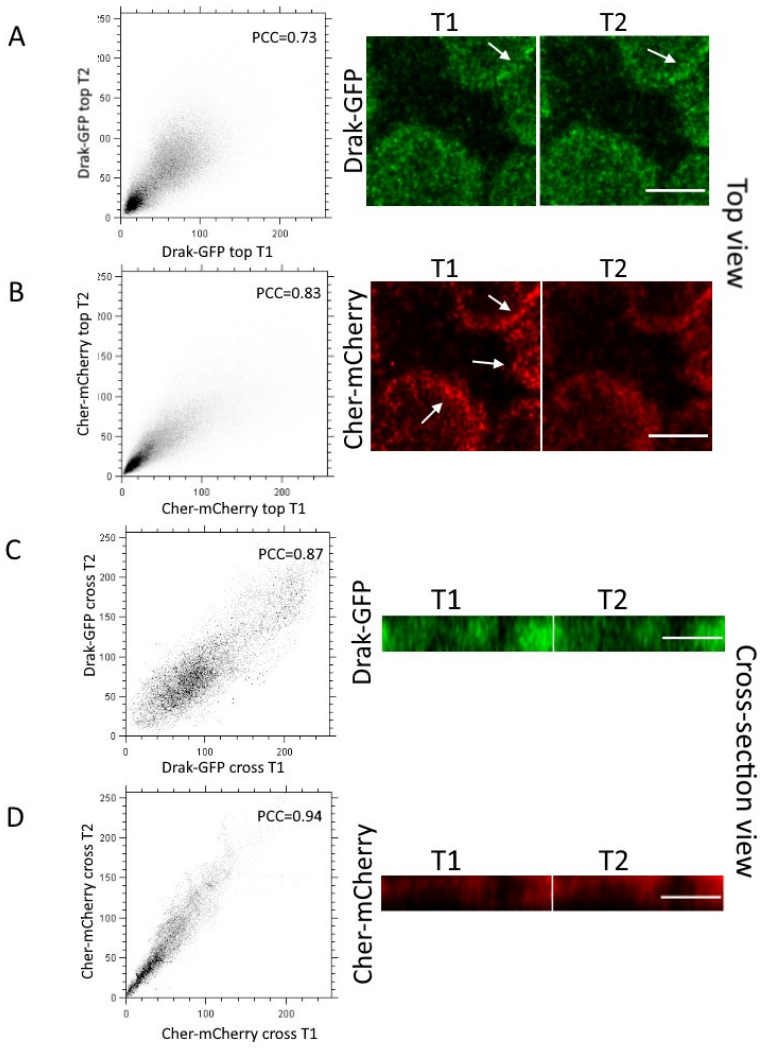

Figure 7. Scatterplots of two consecutively taken Z-stacks from the Drak-GFP;Cher-mCherry fly line. A) Scatterplot of top view of Drak-GFP (T1 and T2). B) Scatterplot of top view of Cher-mCherry (T1 and T2). C) Scatterplot of cross-section view of Drak-GFP (T1 and T2). D) Scatterplot of cross-section view of Cher-mCherry. Top view projections correspond with the cross-section view. PCC was calculated for the whole image. Z-projection size was 2.618 µM. Scale bar was set to 5 µm.

The RBNCC calculation results for the Drak-GFP;Cher-mCherry showed that the uncorrected mean PCC was lower than the corrected (Table 2). Based on the results, the average uncorrected colocalization was 20.7 % lower in the original estimation compared to the corrected colocalization.

TABLE 2. Replicate-based noise corrected correlation (RBNCC) from Drak-GFP;Cher-mCherry. Table contains calculations for both top view (1st row) and the cross-section (2nd row). Average colocalizations were calculated for both Mean (r_{mrg}) and Corrected (r_c). Image quality r_{gg} and r_{rr} is based on self-colocalization from two different timepoints, from which we can calculate the Correction Factor (1). Mean colocalization (r_{mrg}) is an average of four possible estimates from the fluorophores from different timepoints. Average colocalizations were calculated for both Mean (r_{mrg}) and Corrected (r_c).

Drak-GFP;Cher-mCherry

	Image Quality			**Colocalization (PCC) Between Fluorophores**				**Final**	
	r_{gg} (T1-T2)	r_{rr} (T1-T2)	Correction Factor(C_{gr})	r_{g1r1}	r_{g1r2}	r_{g2r1}	r_{g2r2}	Mean (r_{mrg})	Corrected (r_c)
Top	0.731	0.827	1.286	0.627	0.636	0.623	0.656	0.636	0.817
Cross-section	0.867	0.935	1.111	0.545	0.430	0.568	0.471	0.504	0.559
								average colocalizations	
								0.570	0.688

Similarly, Cher-GFP;Sqh-mCherry also showed higher presence of noise within the green channel (Figure 8). This characteristic is more apparent when examining the PCC values in the top view, with both Drak-GFP;Cher-mCherry and Cher-GFP;Sqh-mCherry displaying lower coefficient values in the green channel. This observation implies a higher degree of noise in the green channel. Furthermore, similarly to Drak-GFP;Cher-mCherry red channel, Cher-GFP;Sqh-mCherry T1 looked brighter and had a higher contrast in comparison to T2. Additionally, the nuclei areas in T2 exhibited a heightened background signal.

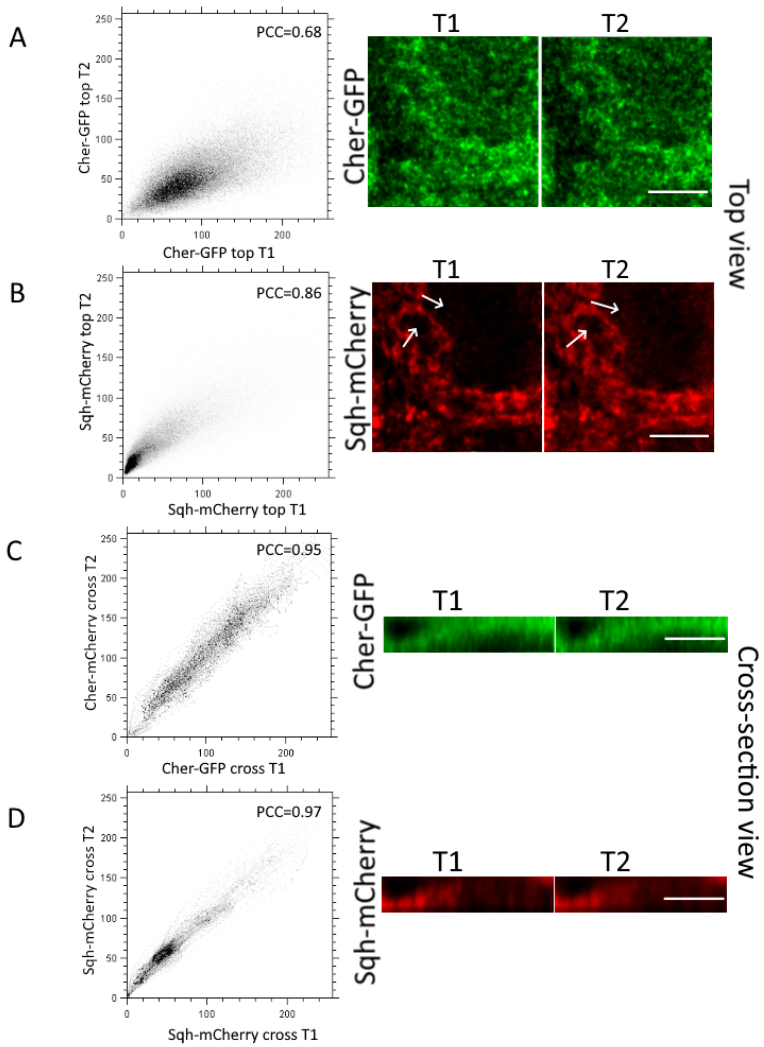

Figure 8. Scatterplots of two consecutively taken Z-stacks from the Cher-GFP;Sqh-mCherry fly line. A) Scatterplot of top view of Cher-GFP (T1 and T2). B) Scatterplot of top view of Sqh-mCherry (T1 and T2). C) Scatterplot of cross-section view of Cher-GFP (T1 and T2). D) Scatterplot of cross-section view of Sqh-mCherry. Top view projections correspond with the cross-section view. Pearson's Correlation Coefficient (PCC) was calculated for the whole image. Z-projection size 2.618 µM. Scale bar was set to 5 µm.

Similarly to the Drak-GFP;Cher-mCherry, the RBNCC calculation results for the Cher-GFP;Sqh-mCherry showed higher average PCC on the corrected (Table 3). The uncorrected average colocalization was 17.8 % lower than the corrected colocalization.

TABLE 3. Replicate-based noise corrected correlation (RBNCC) from Cher-GFP;Sqh-mCherry. Table contains calculations for both top view (first row) and the cross-section (2nd row). Image quality r_{gg} and r_{rr} is based on self-colocalization from two different timepoints, from which we can calculate the Correction Factor (1). Mean colocalization (r_{mrg}) is an average of four possible estimates from the fluorophores from different timepoints. Average colocalizations were calculated for both Mean (r_{mrg}) and Corrected (r_c).

Cher-GFP;Sqh-mCherry

	Image Quality			**Colocalization (PCC) Between Fluorophores**				**Final**	
	r_{gg} (T1-T2)	r_{rr} (T1-T2)	Correction Factor(C_{gr})	r_{g1r1}	r_{g1r2}	r_{g2r1}	r_{g2r2}	Mean (r_{mrg})	Corrected (r_c)
Top	0.676	0.858	1.313	0.511	0.492	0.498	0.538	0.510	0.669
Cross-section	0.950	0.968	1.043	0.465	0.490	0.527	0.566	0.512	0.534
								average colocalizations	
								0.511	0.602

3.5 Manders' Colocalization Coefficient

Manders' Colocalization Coefficient (MCC) measurements were employed to assess whether they yielded results coinciding with PCC. MCC quantifies the percentage of green channel pixels points overlapping with red channel (M1) and the percentage of red channel pixels overlapping with green channel (M2). Notably, MCC differs from PCC in that it does not account for the signal intensity of the two channels and does not care about correlation. MCC measurements were obtained from Drak-GFP control, Cher-GFP;Sqh-mCherry, and Drak-GFP;Cher-mCherry, as they constituted the main focus of this study (Figure 9).

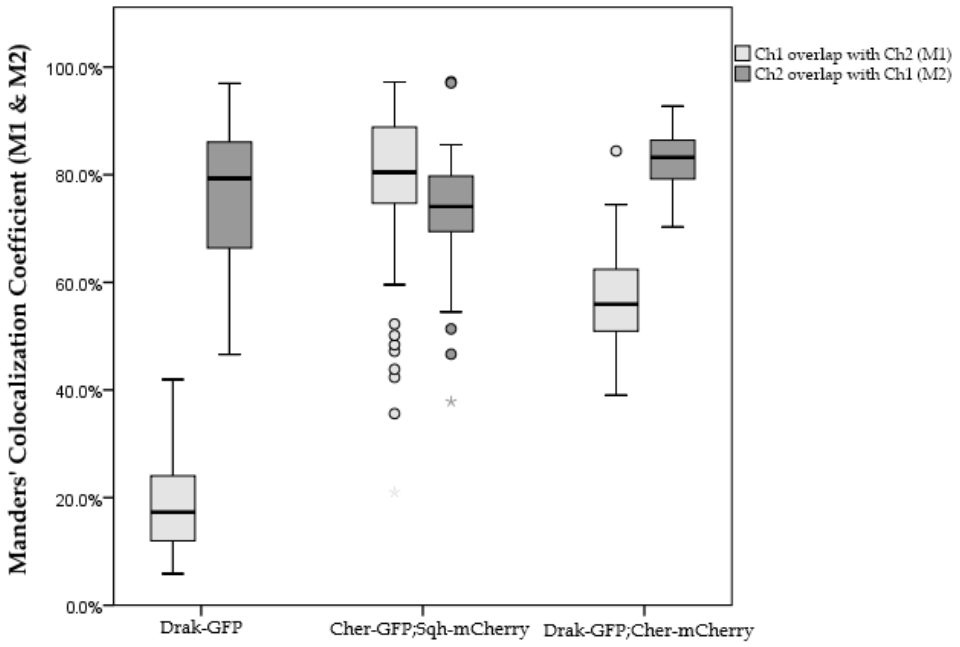

Figure 9. Manders' Colocalization Coefficient (MCC) measurements: x-axis shows the different fly line groups and y-axis shows the MCC values (0 – 1.00) converted to percentage (%). M1 = percentage of Channel 1 pixels overlapping with Channel 2 pixels; M2 = percentage of Channel 2 pixels overlapping with Channel 1 pixels. Boxplot was grouped were M1 = light gray and M2 = dark gray. Control consisted of one fluorophore Drak-GFP. Threshold levels was adjusted manually for both channels for each image.

The MCC measurements yielded the following results: In Drak-GFP, a mean of 18.6 ± 9.2% of Drak-GFP pixels overlapped with those from red channel (M1), while a mean of 76.2 ± 12.9 % of red channel pixels overlapped with Drak-GFP (M2). Cher-GFP;Sqh-mCherry resulted in a mean of 77.4 ± 15.4 % overlap of Cher-GFP with Sqh-mCherry (M1) and 73.2 ± 10.3% overlap of Sqh-mCherry with Cher-GFP (M2). In Drak-GFP;Cher-mCherry, an average of 57.0 ± 8.4% of Drak-GFP overlapped with Cher-mCherry (M1), while an average of 82.6 ± 5.0% of Cher-mCherry overlapped with Drak-GFP (M2).

Drak-GFP control low percentage of overlap between Drak-GFP, and red channel (M1) indicates a lack of overlap as expected. Problem with MCC is the high colocalization value for the M2. The noise pixels and the autofluorescence signals overlapping with the Drak-GFP result in high M2 value. In PCC, this overlap does not produce high value because there is no correlation between the signals.

MCC results from M1 and M2 in Cher-GFP;Sqh-mCherry suggest overlapping between the channels, indicative of colocalization. In Drak-GFP;Cher-mCherry, a high percentage of Cher-mCherry channel overlapped with Drak-GFP (M2), while Drak-GFP resulted in a lower overlap percentage with Cher-GFP (M2). However, the percentage of overlapping Drak-GFP was much higher compared to the control. This implies the presence of colocalization, albeit to a lesser extent compared to Cher-GFP;Sqh-mCherry. These results

somewhat coincide with the observations made in PCC analysis apart from the negative control M2.

3.6 Colocalization degree changes during actin front progression

PCC measurements were plotted against distance from the cortex to the actin front to examine the changes in colocalization during cellularization progression (Figure 10). The plot results confirmed that the PCC measurements for Drak-GFP;Cher-mCherry remained relatively constant throughout the cellularization progression.

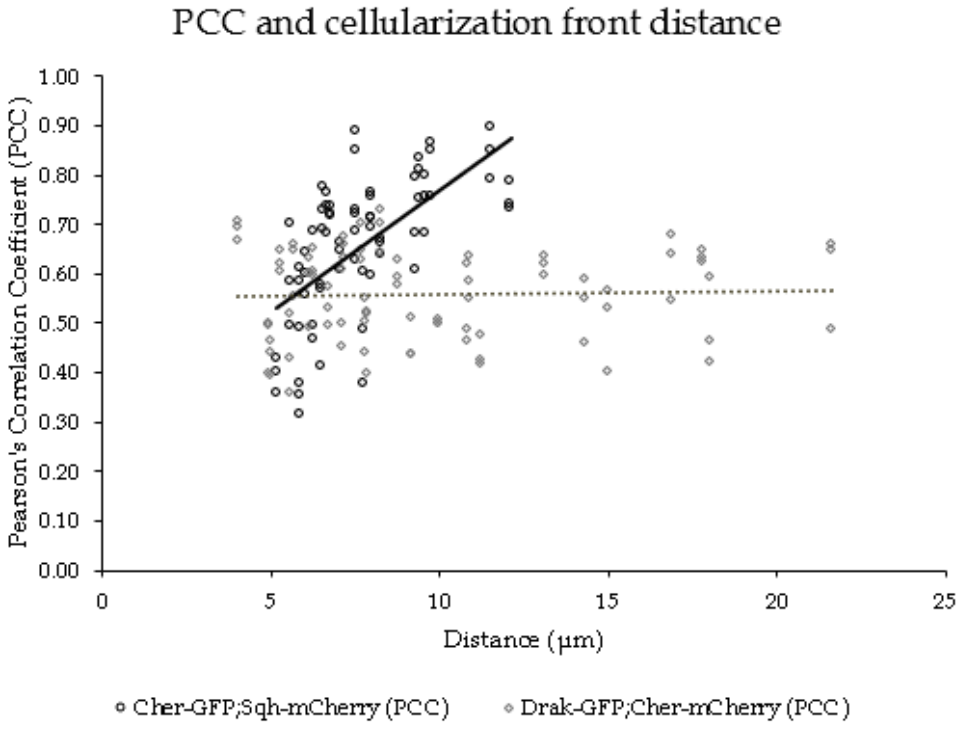

Figure 10. Pearson's Correlation Coefficient and actin front distance from the embryo cortex. X-axis shows the distance of the actin front from the embryo cortex (0-25 µm) while y-axis shows the PCC value from the colocalization measurements.

In contrast, Cher-GFP;Sqh-mCherry displayed a noticeable and consistent increase in PCC values as the actin front advanced (Figure 10). Unfortunately, data from a further distance than ~15 µm are lacking from Cher-GFP;Sqh-mCherry as they were unavailable due to issues associated with Z-shift in the images. However, the results provide clear evidence that the colocalization increases due to the increased activation of Sqh during the progression of cellularization. Similar increase with Drak was not seen.

4 DISCUSSION

The research hypothesis for this study was that if Drak is the main MLCK that regulates the RLC phosphorylation during cellularization, it will colocalize with Cher. If Cher and Drak colocalize simultaneously during cellularization, it would suggest interaction. In this study, I have shown from the live embryo confocal imaging that Drak is recruited to the actin front and localizes with Cher. However, the colocalization degree between Drak and Cher was lower compared to that between Cher and Sqh. Furthermore, the signal intensity from Drak-GFP during cellularization was lower compared to Cher-GFP and Sqh-mCherry. Interestingly, the control Drak-GFP control images showed that at the last nuclear cycles and at the onset of true cellularization, Drak-GFP signal is high near the embryo cortex. This signal remains throughout the cellularization process. Whether Drak colocalizes at the same degree or higher with Cher during this phase remains unclear.

4.1 Drak localizes with Cher at actin front during cellularization

Aim of the study was to see if Drak-GFP localizes to the actin front with Cher-mCherry during cellularization. Results of this study showed that Drak localizes with Cher and comigrates in the actin front during cellularization in early and late phases. However, the image results showed that the colocalization with Cher was not that obvious. Drak signal was initially found mainly on top of the nuclei compartments, after which the Drak-GFP signal followed the actin front together with Cher. The images did not show concentration or increase in signal intensity in the actomyosin ring structure around the nuclei, where Cher signal was most concentrated. Instead, the Drak-GFP signal was evenly distributed throughout the actin front structure. In addition, lower signal of Drak-GFP was observed in the cytosol.

In comparison, Cher-GFP colocalized with Sqh-mCherry in a different manner. Although, Sqh-mCherry showed less colocalization during early phase in the images, its activation increased as the cellularization progressed. Furthermore, Sqh-mCherry was initially localized more throughout the actin front structure similarly to Drak-GFP. However, as the actin front progressed it became more concentrated to the actomyosin ring structures. The differences between Drak-GFP;Cher-mCherry and Cher-GFP;Sqh-mCherry colocalization was well demonstrated in the plot that showed changes in the colocalization degree during cellularization progression (Figure 10). It confirmed the image results, that Drak-GFP and Cher-mCherry colocalization degree did not show any increase throughout the cellularization. In comparison, Cher-GFP and Sqh-mCherry colocalization degree increased. This result support the study by Krueger et al. 2019, which reported that during early phases of cellularization actomyosin fibers are resistant to the Sqh activation. After the actomyosin fibers

arranges to the ring-like conformation, they become sensitive to Sqh activation (Krueger et al. 2019).

The PCC analysis was measured to confirm if there are differences between Drak and Cher colocalization to Cher and Sqh. Welch's independent Student *t*-test was used to see if there are difference between the PCC means. This confirmed that there was statistically significant difference between these groups. Similarly, the MCC results showed lower overlap between Drak and Cher. Both PCC and MCC results along with visual analysis of the images suggest that the colocalization degree between Drak and Cher is lower compared between Cher and Sqh. Although lower, the results indicate that colocalization occurs between Drak and Cher in some degree, suggesting that there might be some interaction. In this study, I was not able to test the colocalization between Drak and Sqh. Unfortunately, a viable homotsygote fly line (Drak-GFP;Sqh-mCherry) was unavailable during this thesis. It might give some clarification about the signaling pathway, whether Drak phosphorylates Sqh directly or through binding to the Cher MSR^{open} site. If Drak colocalizes highly with Sqh, it would suggest that it phosphorylates Sqh RLC directly. If that is not the case, it is possible that Drak act as a recruiter for other MLCK-like kinases. It is my hypothesis that Drak colocalization with Sqh would be higher than it is with Cher as visually it appears to overlap more with Sqh than with Cher. Chougule et al. (2016) discussed the possibility that Drak is required to regulate the function of other kinases that also phosphorylate Sqh during cellularization. Based on the working model by Ylänne J. (Figure 11A), perhaps lack of Drak reduces the initial activation of myosin that forces Cher mechanosensitive region conformation change from closed to open. This could hinder the interaction of Drak with the Cher MSR site, resulting in reduced downstream signaling for other kinases and reduction of Sqh phosphorylation (Figure 11B). Observation by Neubueser and Hipfner (2010) showed that Drak and Rok have overlapping roles. Therefore, it could be that Drak-Cher interaction leads to Rok recruitment to increase the RLC phosphorylation and proper myosin constriction required in the late phases of cellularization. Other candidates might exist as well, as there are many MLCKs that can phosphorylate Sqh (Vicente-Manzarenes et al. 2009). However, if Drak interacts directly with Cher MSR^{open} site it would be assumed that the colocalization degree would increase during cellularization as the myosin constriction causes more conformational change from closed to open. This theory is somewhat contradicted as such increase was not seen in the results (Figure 10).

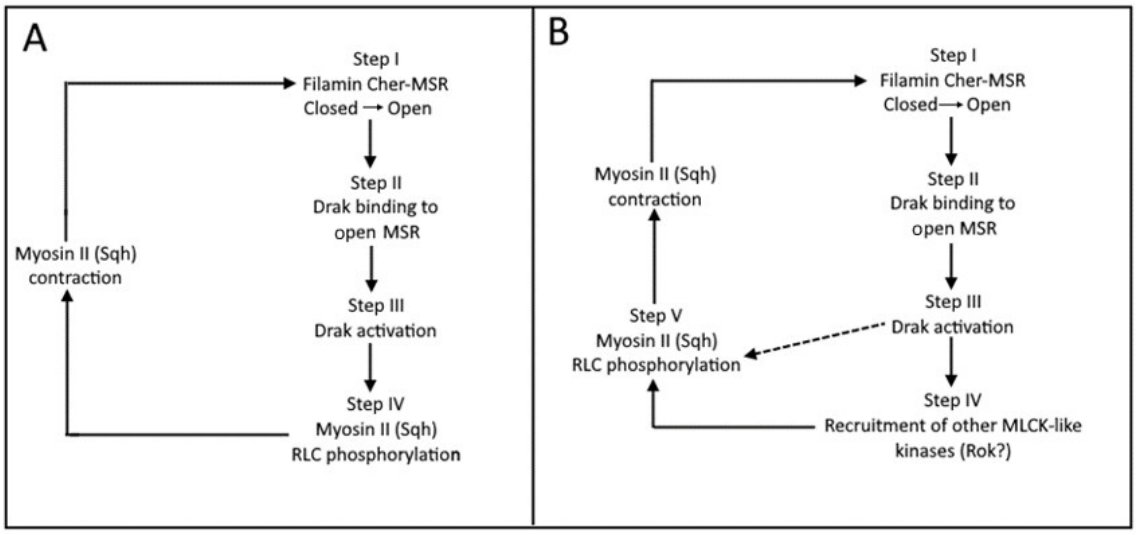

Figure 11. Cher-Drak-Sqh signaling models. A) A working model by Ylänne J., where initiation of myosin activity forces causes actin-crosslinking filamin Cher to be stretched, leading to open MSR conformation (Step I). Open conformation allows Drak -COOH tail interaction with MSR protein binding sites, leading to its activation (Step II and III). Drak activation leads to increase of RLC phosphorylation (Step IV), thus further activating myosin contractile forces. B) Alternative suggestion of a model where Drak activation (Step III) leads to recruitment of other MLCK-like kinases, such as Rok (Step IV). These kinases could then increase RLC phosphorylation and myosin activity either by themselves or in parallel with Drak.

This study revealed that the Drak signal increases at the last nuclear cycles and the priming phase, where the final furrow canals form. Before the nuclei divides, Drak signal is higher and localized to the compartments above the nuclei near the cortex (Figure 7). During nuclear division, the Drak-GFP diffuses to the cytosol perhaps due to lack of nuclear envelopes. Drak signal increases again when new furrows forms between the nuclei. This would suggest that Drak is not needed during nuclear division when microtubules separate the two nuclei apart but is recruited during cortical flow, where new furrow canals form. During that, NM II, actin and other cellular components are also recruited (Figure 12A) (Sokac et al. 2022). It could be that Drak colocalization with Cher is higher during the priming phase, which could mean that it interacts with Cher MSR before true cellularization takes place.

One possibility is that Drak is required for correct coordination. It is known that $Drak^{del}$ and $Drak^{ko}$ mutation causes disorganized furrow canals and wavy actin front, as well as reduced ability to constrict in late phases (Chougule et al. 2016). Furthermore, Drak mutant embryos lead to uneven distribution and clustered NM II (Chougule et al. 2016). Disorganized furrow canals are illustrated in Figure 12B. The reduced ability to constrict in late phases may be due to the unevenly distributed and aggregated NM II with addition to irregular actomyosin ring structures that was discovered by Chougule et al. (2016). These

all could contribute to how the forces generated by NM II are distributed throughout the actomyosin ring structures and lead to a delayed cellularization and reduced ability to constrict in late phase.

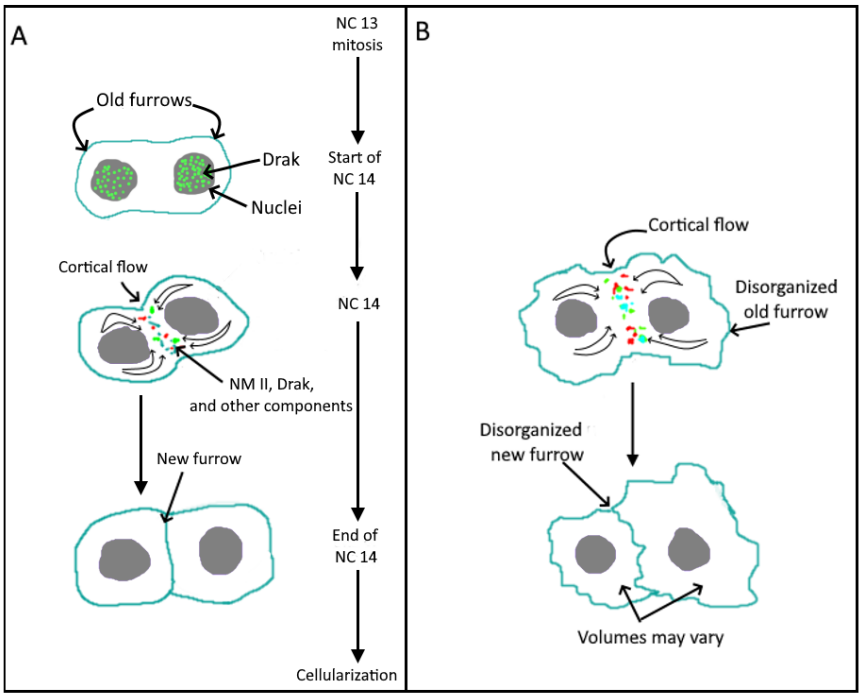

Figure 12. Formation of new furrow canals. A) After the nuclei undergoes nuclear division 13, new furrow canal needs to be formed after the two daughter cells have been pulled to their positions by microtubules (start of nuclear cycle 14). At this stage Drak seems to be localized on top of the nuclei. Due to tension in the middle, cortical flow drives recruitment of NM II and other cellular components, such as Drak, between the two daughter cells. This allows the assembly of the new furrow. B) $Drak^{ko}$ and $Drak^{del}$ mutant flies lead to wavy formation of furrow canals. Disorganization may also lead to varying volume sizes. Figure adapted from Sokac et al. 2023.

Perhaps the lack of Drak leads to disorganization of structures during nuclear cycles and priming phase. Drak might be necessary to coordinate and regulate the phosphorylation of RLC, which is needed to ensure the proper formation of new furrow canals. Disorganized structures could be explained by the reduced mono-phosphorylation, which has been established to enhance adhesion maturation in cellular protrusion (Vicente-Manzaneres and Horwits 2010). Mono-phosphorylation promotes formation of focal adhesion sites, where the cell tightly anchors itself to the ECM and play a critical role in cellular processes, including cell movement and tissue integrity. Since the $Drak^{ko}$ mutant reduces this mono-phosphorylation levels dramatically (84 to 94 %) during cellularization (Chougule et al. 2016), it is possible that it may impair adhesion maturation. This could affect the cellular component's ability to attach correctly to their surroundings and likely lead to a loss of integrity of the furrow membranes and cortical cytoskeleton. Similar cell dynamics was studied with *Drosophila*

ommatidia formation, where the eye formation undergoes several coordinated cell constrictions and adherens junction remodeling (Robertson et al. 2012). The study shows that Drak and Rok function in parallel by phosphorylating Sqh during multicellular alignment and adherens junction remodelling. The ommatidia process requires activation of the epidermal growth factor receptor promoting the exchange of GDP for GTP on GTPases like RhoA. Robertson et al. (2012) suggest that RhoA might regulate the function of Drak, leading to the phosphorylation of NM II along with Rok, driving the multicellular alignment and adherens junction remodelling. Perhaps similar regulation and function could be found during cellularization. Crawford et al.'s (1998) study supports the idea of Rho GTPase as a downstream signal for MLCK-like kinases, as it demonstrated that disrupting Rho GTPase completely halts cellularization and leads to disorganized actomyosin structures. How Drak might interact with Cher during this process remains only speculative as we do not currently have enough data about the colocalization during the last nuclear cycle and formation of new furrow canals. However, it opens a compelling avenue to investigate in the future.

During this project many of the embryos that were imaged were damaged. One of the contributing factors for cellular damage is the requirement of using high-intensity illumination that produces phototoxicity (Tosheva et al. 2020). This is the case especially in live-cell imaging that requires long acquisition times. In fluorescence microscopy one of phototoxic events are due to activating photoactive molecules to reactive states that are able to undergo redox reactions that lead to formation of reactive oxygen stress (ROS). ROS can damage the chemical structure and biological function of biomolecules in their proximity (Laissue et al. 2017, Tosheva et al. 2020).

In this study, embryo survival during the imaging process was assisted by the addition of ascorbic acid to the imaging medium, which functions as an antioxidant. Ascorbic acid and other similar antioxidants have been used in other studies, which have shown reduction in reactive oxygen stress in live cell imaging (Douthwright and Sluder 2017, Harada et al. 2022). Harada et al. (2022) demonstrated that addition of ascorbic acid to the imaging medium yields the best results for live imaging of mitotic processes that are particularly sensitive to phototoxicity. This was also the case in this study, as the addition of ascorbic acid in the imaging medium reduced cellular damage to the embryos, allowing longer acquisition times (data not shown). However, this didn't completely eliminate the problem due to fact that there are always by-products of free radicals from the fluorescence excitation (Laissue et al. 2017). Furthermore, reducing phototoxicity can be difficult as there are many other factors that can contribute to it, such as excitation wavelength, fluorophore concentration, and properties of the organism itself, such as age and development stage (Laissue et al. 2017). For example, the shorter wavelengths, such as blue light (488 nm), has more damaging effect than longer wavelengths (Waters, 2013, Douthwright and Sluder, 2017). It is not ideal to use samples that have been affected by light-induced damage for analysis. Therefore, it is preferable to take steps to further reduce phototoxicity in the future. One simple way to reduce phototoxicity is to reduce

the overall blue light dosage by reducing the intensity of the laser used in the green channel. This could be possible if the Drak-GFP signal could be improved in the future.

During the experiment, Drak-GFP weak signal was a problem that caused difficulties in both imaging and the colocalization analysis. There are many factors that could contribute for the weak signal and such as faulty probe or low expression levels. It is possible that Drak expression levels during early and late cellularization are low, which is why the signal is not strong as Cher or Sqh.

One of the considerations for the low signal-to-noise ratio for the Drak-GFP is the fluorescent tag itself. It is possible that the currently used GFP-tag site in the non-conserved region of the Drak in the C-terminus (Ylänne J. unpublished) might be causing problems. It is possible that the current GFP-tag insertion is unstable and might be cut off from the protein resulting in unwanted signals in the cytosol. If this is the case, the true Drak signal is difficult to discriminate from the background signal and affect the reliability of the colocalization analysis as well. Improvements could be achieved if a more optimal insertion site could be discovered in the future. The fluorescent protein marker could be inserted to the N-terminal or alternatively, inserted to the coding sequence, to a site that does not affect the functionality of the protein, such as correct folding (Snapp 2005). Other consideration that might affect the protein correct function is the properties of the fluorescent protein itself. Fluorescent proteins such as GFP are not that small (~27 kDa) which represents a significant addition to the protein. This may affect correct folding, function, or targeting (Snapp 2005).

Improvements to the weak signal issues can also be alleviated with image processing. The original quality of the image is not an exact representation due to factors such as non-spherical point spread function (PSF), single photon hits, and stray light that can add intensities that contribute to the background, leading to noise and fluctuations (Landmann and Marbet 2004). These reduces image quality by obscuring low-intensity details. If there is a low-contrast, the background and noise can contribute heavily to the maximum intensity, limiting analysis to only high-intensity ranges in raw images. To expand the intensity range for analysis, Landmann and Marbet (2004) recommends using image processing techniques to enhance the signal-to-noise ratio.

Noise reduction can be achieved by using different filters, such as low pass, median, or Gaussian filters (Landmann and Marbet 2004). However, these reduce noise at the expense of resolution. The procedure causes the background to be merged with and distributed over signal and can cause artifacts, which can lead to inaccurate results. Alternatively, a superior image processing method to correct the blurriness and noise without affecting the resolution is the deconvolution.

This image processing technique helps improving image quality by reassigning the captured out-of-focus light back to its original position and increase signal-to-noise ratio (McNally et al. 1999). Deconvolution processing reduces blur by using imaging properties of the optical system in the form of the

point spread function (PSF) (McNally et al. 1999). In this thesis, deconvolution method was better solution for image processing than the filtering techniques, as reduction of the resolution in colocalization analysis is undesirable. This processing technique provided adequate results. This was well demonstrated in this thesis where the unprocessed raw images contained a lot of background noise, and structures were harder to distinguish (Appendix 1). The deconvolution processing technique improved the visibility of structures in the produced images by increasing contrast and reducing noise (Appendix 1). Similar results have been achieved in many other studies (McNally et al. 1999, Landmann and Marbet 2004). Deconvolution processing also improved considerably the results of the PCC as well (Appendix 2).

Although image processing can help reduce the noise it can still affect the analysis. Comparison of the PCC result of the same channel from the fixed embryos showed that in both channels, there were deviation from the expected PCC value (1.0), which indicated the presence of noise and its effect on analysis. The effect of noise to the analysis can be considered by calculating the replicate-based noise corrected correlation (RBNCC) (Adler et al. 2008). Based on the calculated correction factor for Drak-GFP;Cher-mCherry (Table 2) and Cher-GFP;Sqh-mCherry (Table 3), the colocalization degree is higher than the non-corrected. Although I was only able to apply the correction factor to fixed embryo, as this was not done for the live embryos, the results imply that the true colocalization degree is most likely higher than reported in Figure 8 and Appendix 4. This is most likely the case because Adler et al. (2008) argues that the measured PCC is generally understated from the true PCC. The results showed that there was an approximately 17-20 % difference between the non-corrected and corrected. Even in apparently high-quality images, they found that there is around an average of 20 % discrepancy between the measured and corrected colocalization (Adler et al. 2008). Considering this, it could be preferable to calculate the RBNCC for the live imaging of the embryos in the future. However, other factors could have also affected why there was a deficit in PCC value between the T1 and T2 channels. For example, the results can be affected by a slight drift in the sample, which the RBNCC cannot remedy. However, this was unlikely the case as only one fixed embryo was imaged at a time, thus reducing the movement of the confocal lens and the mounted sample.

4.2 An array of choices in colocalization analysis methods

While visual representation of colocalization is crucial part of the qualitative analysis, sometimes it is difficult to tell whether the two probes are truly colocalized. For example, in this study Cher-mCherry fluorescence signal was relatively high compared to the Drak-GFP, causing the signal to be obstructed in the merged image. Moreover, the difference between the optical microscopy

diffraction resolution limit and the size of the proteins of interest can lead to misinterpretations (Comeau et al. 2006). Several quantitative methods that measure colocalization degree in biological microscopy have been developed to address this issue. The method of choice depends on several factors, such as the biological research question and the characteristics of the images. However, the choice of method for analyzing colocalization can be tricky as no single method can fully capture the complexity of colocalization.

Two commonly used methods are the PCC and MCC (Dunn et al. 2011), which were also used in this thesis. Although both methods measure the colocalization degree, each approach has its own set of advantages and disadvantages. However, one should not be considered superior over the other. PCC measures the linear correlation between the intensities of the two fluorophores, while MCC measures the proportion of each fluorophore that overlaps with the other (Dunn et al. 2011). Unlike PCC, MCC is independent of signal proportionality, but it is sensitive to co-occurrence, and it does not care about correlation. MCC is also very sensitive to threshold levels, which is complicated by the background noise in the images. This was the case in this study, where the background signal in Drak-GFP control red channel showed high overlap with green channel. High coefficient value is explained by the background noise pixels overlapping with Drak-GFP causing false-positive colocalization. This result indicates that for MCC analysis, choosing a negative control from an embryo that expresses two probes known to be non-coincident during cellularization could be a better option than using embryo expressing single probe. Similar high colocalization in negative controls was not observed in PCC. Additionally, adjusting and selecting the threshold levels by manually introduces easily human biases. Automatic methods such as Costes' automatic threshold method are preferred to solve this problem. (Costes et al. 2004). Nevertheless, it is essential to visually examine and evaluate the outcomes of Costes' automatic thresholding (Dunn et al. 2011). This would have proven to be a time-consuming process as in time-lapse images the dataset was substantial. Furthermore, studies have shown that in certain conditions, the Costes' method can fail to produce a threshold level that is usable. Comeau et al. 2006 showed that Costes' method can have a hard time finding appropriate threshold level, especially if there is a very high particle density. While the Costes' method can be very effective for images with high signal-to-background ratios, for low signal levels, it can set threshold values so low that it fails to discriminate labelled structures from the background (Dunn et al. 2011). Similarly, this held true in several of the images I tested. The Costes' automatic threshold would underestimate the threshold level incorrectly as it would fail to separate the background from the signal (data not shown). This is why, in this study, the threshold was set manually for the MCC, which unfortunately introduced inaccuracies for the measurements. If the signal-to-background could be increased and the noise reduced further in the future, the MCC could be more useful tool for analysis. Unlike the MCC, PCC is very straightforward and well-defined metric that is notably unaffected by the researcher's biases. For these

reasons, PCC was used for statistical analysis over MCC in this study. Another interesting technique to measure colocalization is to use image cross-correlation spectroscopy (ICCS), which also functions well even if the particle density is high (Comeau et al. 2006). The ICCS is proved to give far more accurate than the more commonly used colocalization analysis methods (Comeau et al. 2008). Thus, it is a technique that could be considered in the future.

It is also important considering other methods as a means of validating our results. While this study statistical analysis of PCC showed degree of colocalization, it does not necessarily mean that the proteins interact with certainty due to resolution restrictions. The fluorescence microscope resolution is limited to several hundred nanometers, while the proteins might only be few nanometers in size (Piston and Kremers 2007). This meaning that a typical fluorescence imaging experiment can only yield information that the two proteins are in close proximity. Protein-protein interaction have been historically studied with immunofluorescence microscopy *in situ*. Other method that is commonly used is electron microscopy, which offers the needed resolution. However, the problem with electron microscopy is that it lacks precise labelling strategies. Both methods also share the drawback of being limited to fixed cells (Piston and Kremers 2007). Other promising method that could be used is fluorescence resonance energy transfer (FRET) (Truong and Ikura 2001, Piston and Kremers 2007), which provides high spatial resolution assays on protein-protein interactions and can also detect conformational changes *in vivo*. This offers advantage over other methods, as dynamic molecular events can be tracked in living cells. However, FRET usually performed only when the particle density is low (Comeau et al. 2008), thus in this case, ICCS might be better solution. However, high-resolution methods could increase the confidence in the colocalization measurements shown in this thesis, providing more comprehensive understanding of the molecular interactions and functions of Drak and Cher.

4.3 Conclusions

Visual and measured colocalization analyses demonstrated that Drak comigrates along with Cher and localizes along the actin front. In contrast to Cher-Sqh colocalization, PCC analysis showed a lower degree of Drak-Cher colocalization. Drak's colocalization did not increase with cellularization compared to Sqh's. These results partly contradict the working model where Drak binds to the Cher MSR^{open} region to activate Drak. However, the results showed that the Drak-GFP fluorescence signal increased between the last nuclear cycles and at the onset of true cellularization ("priming phase"). The Drak signal is localized on top of the nuclei near the cellular cortex and present in the cortical flow, where a new furrow canal forms. Drak interaction with the Cher MSR site may occur before cellularization takes place. One possible theory is that Drak has a central role in forming the correct assembly and promoting membrane integrity through adhesion maturation. Due to the lack of colocalization data during the priming

phase, this is unknown, but it is a compelling avenue for further research. Considering all the results, it is unclear whether Drak interacts with Cher MSR^{open}, even though there is evidence that Drak colocalizes with Cher to some degree during cellularization. Due to the problems faced in this thesis, such as the low Drak-GFP signal and the signal-to-noise ratio, the results might not fully represent the whole picture. Use of high-resolution imaging techniques, such as FRET, or a more accurate method of colocalization analysis, such as image cross-correlation, could be considered for validation of the results. Lastly, this thesis has advanced our knowledge of filamin's mechanically regulated signaling pathways while also prompting intriguing questions that warrant further investigation.

ACKNOWLEDGEMENTS

I would like to express my gratitude to my supervisor, professor Jari Ylänne, for his support and for allowing me to be a part of his research project, "The function of filamin as a mechanosensor in muscle development and muscle diseases". Being a part of this research project was an enlightening experience that significantly contributed to my academic and professional growth. I am also thankful to the Academy of Finland for their financial support, which made this study possible.

Jyväskylä November 11, 2023
Panu Tapio Siipilehto

REFERENCES

Adler J., Pagakis S.N. & Parmryd I. 2008. Replicate-based noise corrected correlation for accurate measurements of colocalization. *J Microsc.* 230: 121–133.

Afshar K., Stuart B. & Wasserman S.A. 2000. Role of Diaphanous FH protein in early embryonic development. *Development* 127: 1887–1897.

Bao G. & Suresh S. 2003. Cell and molecular mechanics of biological materials. *Nat Mater.* 2: 715–725.

Bello N.F., Lamsoul I., Heuzé M.L., Métais A., Moreaux G., Calderwood D.A., Duprez D., Moog-Lutz C. & Lutz P.G. 2009. The E3 ubiquitin ligase specificity subunit ASB2β is a novel regulator of muscle differentiation that targets filamin B to proteasomal degradation. *Cell Death Differ.*16: 921–932.

Betapudi V. 2014. Life without double-headed non-muscle myosin II motor proteins. *Front Chem.* 2, doi: 10.3389/fchem.2014.00045.

Betapudi V., Licate L.S. & Egelhoff T.T. 2006. Distinct roles of nonmuscle myosin II isoforms in the regulation of MDA-MB-231 breast cancer cell spreading and migration. *Cancer Res.* 66: 4725–4733.

Bray D. & White J.G. 1988. Cortical flow in animal cells. *Science* 239: 883–888.

Chougule A.B., Hastert M.C. & Thomas J.H. 2016. Drak is required for actomyosin organization during *Drosophila* cellularization. *G3: Genes Genomes Genet.* 6: 819–828.

Clark K., Langeslag M., Figdor C.G. & Leeuwen F.N. van. 2007. Myosin II and mechanotransduction: a balancing act. *Trends Cell Biol.* 17: 178–186.

Comeau J.W.D., Costantino S. & Wiseman P.W. 2006. A guide to accurate fluorescence microscopy colocalization measurements. *Biophys J.* 91: 4611–4622.

Comeau J.W.D., Kolin D.L. & Wiseman P.W. 2008. Accurate measurements of protein interactions in cells via improved spatial image cross-correlation spectroscopy. *Mol BioSyst.* 4: 672.

Conti M.A., Even-Ram S., Liu C., Yamada K.M. & Adelstein R.S. 2004. Defects in cell adhesion and the visceral endoderm following ablation of nonmuscle myosin heavy chain II-A in Mice. *J Biol Chem.* 279: 41263–41266.

Costes S.V., Daelemans D., Cho E.H., Dobbin Z., Pavlakis G. & Lockett S. 2004. Automatic and quantitative measurement of protein-protein colocalization in live cells. *Biophys J.* 86: 3993–4003.

Crawford J.M., Harden N., Leung T., Lim L. & Kiehart D.P. 1998. Cellularization in *Drosophila melanogaster* is disrupted by the inhibition of Rho activity and the activation of Cdc42 function. *Dev Biol.* 204: 151–164.

Cunningham C.C., Gorlin J.B., Kwiatkowski D.J., Hartwig J.H., Janmey P.A., Byers H.R. & Stossel T.P. 1992. Actin-binding protein requirement for cortical stability and efficient locomotion. *Science* 255: 325–327.

D'Addario M., Arora P.D., Ellen R.P. & McCulloch C.A.G. 2002. Interaction of p38 and Sp1 in a mechanical force-induced, β1 Integrin-mediated

transcriptional circuit that regulates the actin-binding protein Filamin-A. *J Biol Chem.* 277: 47541–47550.

D'Addario M., Arora P.D., Fan J., Ganss B., Ellen R.P. & McCulloch C.A.G. 2001. Cytoprotection against mechanical forces delivered through β1 integrins requires induction of Filamin A. *J Biol Chem.* 276: 31969–31977.

Dean S.O. & Spudich J.A. 2006. Rho kinase's role in myosin recruitment to the equatorial cortex of mitotic *Drosophila* S2 cells is for myosin regulatory light chain phosphorylation. *PLoS ONE* 1: e131, doi: 10.1371/journal.pone.0000131.

Douthwright S. & Sluder G. 2017. Live cell imaging: assessing the phototoxicity of 488 and 546 nm light and methods to alleviate it. *J Cell Physiol.* 232: 2461–2468.

Dunn K.W., Kamocka M.M. & McDonald J.H. 2011. A practical guide to evaluating colocalization in biological microscopy. *Am J Physiol Cell Physiol.* 300: C723–C742.

Figard L., Xu H., Garcia H.G., Golding I. & Sokac A.M. 2013. The plasma membrane flattens out to fuel cell-surface growth during *Drosophila* cellularization. *Dev Cell.* 27: 648–655.

Foe V.E. & Alberts B.M. 1983. Studies of nuclear and cytoplasmic behaviour during the five mitotic cycles that precede gastrulation in *Drosophila* embryogenesis. *J Cell Sci.* 61: 31–70.

Fürst D.O., Goldfarb L.G., Kley R.A., Vorgerd M., Olivé M. & Ven P.F.M. van der. 2013. Filamin C-related myopathies: pathology and mechanisms. *Acta Neuropathol.* 125: 33–46.

Gehler S., Baldassarre M., Lad Y., Leight J.L., Wozniak M.A., Riching K.M., Eliceiri K.W., Weaver V.M., Calderwood D.A. & Keely P.J. 2009. Filamin A–beta1 integrin complex tunes epithelial cell response to matrix tension. *Mol Biol Cell.* 20.

Glogauer M., Arora P., Chou D., Janmey P.A., Downey G.P. & McCulloch C.A.G. 1998. The role of actin-binding protein 280 in integrin-dependent mechanoprotection. *J Biol Chem.* 273: 1689–1698.

Gorlin J.B., Yamin R., Egan S., Stewart M., Stossel T.P., Kwiatkowski D.J. & Hartwig J.H. 1990. Human endothelial actin-binding protein (ABP-280, nonmuscle filamin): a molecular leaf spring. *J Cell Biol.* 111: 1089–1105.

Großhans J., Wenzl C., Herz H.-M., Bartoszewski S., Schnorrer F., Vogt N., Schwarz H. & Müller H.-A. 2005. RhoGEF2 and the formin Dia control the formation of the furrow canal by directed actin assembly during *Drosophila* cellularisation. *Development* 132: 1009–1020.

Hales K.G., Korey C.A., Larracuente A.M. & Roberts D.M. 2015. Genetics on the fly: a primer on the *Drosophila* Model System. *Genetics* 201: 815–842.

Harada T., Hata S., Fukuyama M., Chinen T. & Kitagawa D. 2022. An antioxidant screen identifies ascorbic acid for prevention of light-induced mitotic prolongation in live cell imaging. *bioRxiv.* doi: 10.1101/2022.06.20.496814

He B., Martin A. & Wieschaus E. 2016. Flow-dependent myosin recruitment

during *Drosophila* cellularization requires zygotic *dunk* activity. *Development*: dev.131334.

Heikkinen O.K., Ruskamo S., Konarev P.V., Svergun D.I., Iivanainen T., Heikkinen S.M., Permi P., Koskela H., Kilpeläinen I. & Ylänne J. 2009. Atomic structures of two novel immunoglobulin-like domain pairs in the actin cross-linking protein Filamin. *J Biol Chem.* 284: 25450–25458.

Heissler S.M. & Sellers J.R. 2014. Myosin light chains: Teaching old dogs new tricks. *BioArchitecture* 4: 169–188.

Hoffman B.D., Grashoff C. & Schwartz M.A. 2011. Dynamic molecular processes mediate cellular mechanotransduction. *Nature* 475: 316–323.

Houdusse A., Kalabokis V.N., Himmel D. & Cohen C. Atomic structure of scallop myosin subfragment S1 complexed with MgADP: a novel conformation of the myosin head. *Cell*. 97: 459–470.

Huelsmann S., Rintanen N., Sethi R., Brown N.H. & Ylänne J. 2016. Evidence for the mechanosensor function of filamin in tissue development. *Sci Rep* 6: 32798, doi: 10.1038/srep32798.

Icha J., Weber M., Waters J.C. & Norden C. 2017. Phototoxicity in live fluorescence microscopy, and how to avoid it. *BioEssays* 39: 1700003, doi: 10.1002/bies.201700003.

Izquierdo E., Quinkler T. & De Renzis S. 2018. Guided morphogenesis through optogenetic activation of Rho signalling during early *Drosophila* embryogenesis. *Nat Commun.* 9: 2366.

Jordan P. & Karess R. 1997. Myosin light chain–activating phosphorylation sites are required for oogenesis in *Drosophila*. *J Cell Biol.* 139: 1805–1819.

Kainulainen T., Pender A., D'Addario M., Feng Y., Lekic P. & McCulloch C.A. 2002. Cell death and mechanoprotection by Filamin A in connective tissues after challenge by applied tensile forces. *J Biol Chem.* 277: 21998–22009.

Karess R.E., Chang X., Edwards K.A., Aguilera I. & Kiehartt D.P. 1991. The regulatory light chain of nonmuscle myosin is encoded by spaghetti-squash, a gene required for cytokinesis in *Drosophila*. *Cell.* 65: 1177–1189.

Kley R.A., Serdaroglu-Oflazer P., Leber Y., Odgerel Z., Ven P.F.M. van der, Olivé M., Ferrer I., Onipe A., Mihaylov M., Bilbao J.M., Lee H.S., Höhfeld J., Djinović-Carugo K., Kong K., Tegenthoff M., Peters S.A., Stenzel W., Vorgerd M., Goldfarb L.G. & Fürst D.O. 2012. Pathophysiology of protein aggregation and extended phenotyping in filaminopathy. *Brain* 135: 2642–2660.

Krakow D., Robertson S.P., King L.M., Morgan T., Sebald E.T., Bertolotto C., Wachsmann-Hogiu S., Acuna D., Shapiro S.S., Takafuta T., Aftimos S., Kim C.A., Firth H., Steiner C.E., Cormier-Daire V., Superti-Furga A., Bonafe L., Graham J.M., Grix A., Bacino C.A., Allanson J., Bialer M.G., Lachman R.S., Rimoin D.L. & Cohn D.H. 2004. Mutations in the gene encoding filamin B disrupt vertebral segmentation, joint formation and skeletogenesis. *Nat Genet.* 36: 405–410.

Krueger D., Quinkler T., Mortensen S.A., Sachse C. & De Renzis S. 2019. cross-

linker–mediated regulation of actin network organization controls tissue morphogenesis. *J Cell Biol.* 218: 2743–2761.
Kuo J.-C., Lin J.-R., Staddon J.M., Hosoya H. & Chen R.-H. 2003. Uncoordinated regulation of stress fibers and focal adhesions by DAP kinase. *J Cell Sci.* 116: 4777–4790.
Lad Y., Kiema T., Jiang P., Pentikäinen O.T., Coles C.H., Campbell I.D., Calderwood D.A. & Ylänne J. 2007. Structure of three tandem filamin domains reveals auto-inhibition of ligand binding. *EMBO J.* 26: 3993–4004.
Laissue P.P., Alghamdi R.A., Tomancak P., Reynaud E.G. & Shroff H. 2017. Assessing phototoxicity in live fluorescence imaging. *Nat Met.* 14: 657–661.
Landmann L. & Marbet P. 2004. Colocalization analysis yields superior results after image restoration. *Microsc Res Tech.* 64: 103–112.
Lecuit T. & Lenne P.-F. 2007. Cell surface mechanics and the control of cell shape, tissue patterns and morphogenesis. *Nat Rev Mol Cell Biol.* 8: 633–644.
Lecuit T. & Wieschaus E. 2000. Polarized insertion of new membrane from a cytoplasmic reservoir during cleavage of the *Drosophila* embryo. *J Cell Biol.*150: 849–860.
Leica Microsystems. 2023. Leica TCS SP8 HYD Brochure. (accessed 08.10.2023) https://www.umassmed.edu/globalassets/three-dimensional-microscopy/files/resources/leica-tcs_sp8_hyd-brochure_en.pdf
Li M., Serr M., Edwards K., Ludmann S., Yamamoto D., Tilney L.G., Field C.M. & Hays T.S. 1999. Filamin is required for ring canal assembly and actin organization during *Drosophila* Oogenesis. *J Cell Biol.*146: 1061–1074.
Lu J., Lian G., Lenkinski R., De Grand A., Vaid R.R., Bryce T., Stasenko M., Boskey A., Walsh C. & Sheen V. 2007. Filamin B mutations cause chondrocyte defects in skeletal development. *Hum Mol Genet.* 16: 1661–1675.
Ma X., Kovács M., Conti M.A., Wang A., Zhang Y., Sellers J.R. & Adelstein R.S. 2012. Nonmuscle myosin II exerts tension but does not translocate actin in vertebrate cytokinesis. *Proc Natl Acad Sci U.S.A.* 109: 4509–4514.
Mazumdar A. & Mazumdar M. 2002. How one becomes many: blastoderm cellularization in *Drosophila melanogaster*. *BioEssays* 24: 1012–1022.
McNally J.G., Karpova T., Cooper J. & Conchello J.A. 1999. Three-dimensional imaging by deconvolution microscopy. *Methods* 19: 373–385.
Minestrini G., Harley A.S. & Glover D.M. 2003. Localization of Pavarotti-KLP in living *Drosophila* embryos suggests roles in reorganizing the cortical cytoskeleton during the mitotic cycle V. *Mol Biol Cell.* 14: 4028-4038
Murata-Hori M., Suizu F., Iwasaki T., Kikuchi A. & Hosoya H. 1999. ZIP kinase identified as a novel myosin regulatory light chain kinase in HeLa cells. *FEBS Letters* 451: 81–84.
Nakamura F., Stossel T.P. & Hartwig J.H. 2011. The filamins: organizers of cell structure and function. *Cell Adh Migr.* 5: 160–169.
Neubueser D. & Hipfner D.R. 2010. Overlapping roles of *Drosophila* Drak and Rok kinases in epithelial tissue morphogenesis. *MBoC.* 21: 2869–2879.
Oria R., Wiegand T., Escribano J., Elosegui-Artola A., Uriarte J.J., Moreno-

Pulido C., Platzman I., Delcanale P., Albertazzi L., Navajas D., Trepat X., García-Aznar J.M., Cavalcanti-Adam E.A. & Roca-Cusachs P. 2017. Force loading explains spatial sensing of ligands by cells. *Nature* 552: 219–224.

Piston D.W. & Kremers G.-J. 2007. Fluorescent protein FRET: the good, the bad and the ugly. *Trends Biochem Sci.* 32: 407–414.

Popowicz G.M., Schleicher M., Noegel A.A. & Holak T.A. 2006. Filamins: promiscuous organizers of the cytoskeleton. *Trends Biochem Sci.* 31: 411–419.

Pudas R., Kiema T.-R., Butler P.J.G., Stewart M. & Ylänne J. 2005. Structural basis for vertebrate filamin dimerization. *Structure* 13: 111–119.

Quintin S., Gally C. & Labouesse M. 2008. Epithelial morphogenesis in embryos: asymmetries, motors and brakes. *Trends Genet.* 24: 221–230.

Razinia Z., Mäkelä T., Ylänne J. & Calderwood D.A. 2012. Filamins in mechanosensing and signaling. *Annu Rev Biophys.* 41: 227–246.

Reymann A.-C., Staniscia F., Erzberger A., Salbreux G. & Grill S.W. 2016. Cortical flow aligns actin filaments to form a furrow. *eLife* 5, e17807, doi: 10.7554/eLife.17807.

Robertson F., Pinal N., Fichelson P. & Pichaud F. 2012. Atonal and EGFR signalling orchestrate *rok*- and *Drak*-dependent adherens junction remodelling during ommatidia morphogenesis. *Development* 139: 3432–3441.

Robinson D.N., Smith-Leiker T.A., Sokol N.S., Hudson A.M. & Cooley L. 1997. Formation of the *Drosophila* ovarian ring canal inner rim depends on *cheerio*. *Genetics* 145: 1063–1072.

Rognoni L., Stigler J., Pelz B., Ylänne J. & Rief M. 2012. Dynamic force sensing of filamin revealed in single-molecule experiments. *Proc Natl Acad Sci U.S.A.* 109: 19679–19684.

Schindelin J., Arganda-Carreras I., Frise E., Kaynig V., Longair M., Pietzsch T., Preibisch S., Rueden C., Saalfeld S., Schmid B., Tinevez J.-Y., White D.J., Hartenstein V., Eliceiri K., Tomancak P. & Cardona A. 2012. Fiji: an open-source platform for biological-image analysis. *Nat Methods* 9: 676–682.

Shewan A.M., Maddugoda M., Kraemer A., Stehbens S.J., Verma S., Kovacs E.M. & Yap A.S. 2005. Myosin 2 is a key Rho kinase target necessary for the local concentration of E-cadherin at cell–cell contacts. *Mol Biol Cell.* 16: 4531–4542.

Shutova M.S. & Svitkina T.M. 2018. Mammalian nonmuscle myosin II comes in three flavors. *Biochem Biophys Res Commun.* 506: 394–402.

Singh K., Kim A.B. & Morgan K.G. 2021. Non-muscle myosin II regulates aortic stiffness through effects on specific focal adhesion proteins and the non-muscle cortical cytoskeleton. *J Cell Mol Med.* 25: 2471–2483.

Sokac A.M., Biel N. & De Renzis S. 2023. Membrane-actin interactions in morphogenesis: Lessons learned from *Drosophila* cellularization. *Semin Cell Dev Biol.* 133: 107–122.

Sokol N.S. & Cooley L. 1999. *Drosophila* filamin encoded by the cheerio locus is a component of ovarian ring canals. *Curr Biol.* 9: 1221–1230.

Stossel T.P., Condeelis J., Cooley L., Hartwig J.H., Noegel A., Schleicher M. & Shapiro S.S. 2001. Filamins as integrators of cell mechanics and signalling. *Nat Rev Mol Cell Biol.* 2: 138–145.

Tosheva K.L., Yuan Y., Matos Pereira P., Culley S. & Henriques R. 2020. Between life and death: strategies to reduce phototoxicity in super-resolution microscopy. *J Phys D Appl Phys.* 53, 163001, doi: 10.1088/1361-6463/ab6b95.

Truong K. & Ikura M. 2001. The use of FRET imaging microscopy to detect protein–protein interactions and protein conformational changes *in vivo*. *Curr Opin Struct Biol.* 11: 573–578.

Ueda K., Murata-Hori M., Tatsuka M. & Hosoya H. 2002. Rho-kinase contributes to diphosphorylation of myosin II regulatory light chain in nonmuscle cells. *Oncogene* 21: 5852–5860.

Warn R.M. & Robert-Nicoud M. 1990 F-actin organization during the cellularization of the Drosophila embryo as revealed with a confocal laser scanning microscope. *J Cell Sci.* 96: 35–42

Vasquez C.G., Heissler S.M., Billington N., Sellers J.R. & Martin A.C. 2016. *Drosophila* non-muscle myosin II motor activity determines the rate of tissue folding. *eLife* 5, e20828, doi: 10.7554/eLife.20828.

Waters J.C. 2013. Live-Cell fluorescence imaging. In: *Methods in Cell Biol.* Elsevier, pp. 146–147.

Vicente-Manzanares M. & Horwitz A.R. 2010. Myosin light chain mono- and di-phosphorylation differentially regulate adhesion and polarity in migrating cells. *Biochem Biophys Res Commun.* 402: 537–542.

Vicente-Manzanares M., Ma X., Adelstein R.S. & Horwitz A.R. 2009. Non-muscle myosin II takes centre stage in cell adhesion and migration. *Nat Rev Mol Cell Biol.* 10: 778–790.

Vogel V. & Sheetz M. 2006. Local force and geometry sensing regulate cell functions *Nat Rev Mol Cell Biol.* 7: 265–275.

Zhou X., Borén J. & Akyürek L.M. 2007. Filamins in cardiovascular development. *Trends Cardiovasc Med.* 17: 222–229.

APPENDIX 1 DECONVOLUTION IMAGE PROCESSING

To study Drak localization in each *Drosophila* embryos, a fly line with GFP insertion to Drak gene was imaged. GFP intensity was observable but relatively weak and mainly cytoplasmic. With Lighting / Thunder deconvolution image processing the signal-to-noise ratio was increased and quality in images was improved (Appendix 1) along with colocalization analysis (Appendix 2). Raw images exhibited unwanted signal, particularly in the Drak-GFP channel. For example, we can see signal in the nuclei areas (darker regions) where there shouldn't be signal. Moreover, the low image contrast rendered many details unclear. Employing deconvolution image processing technique, image contrast was effectively enhanced, and background signal was reduced. Consequently, this processing increased the level of detail in the images, rendering features such as nuclei (dark regions) and actin front more distinguishable.

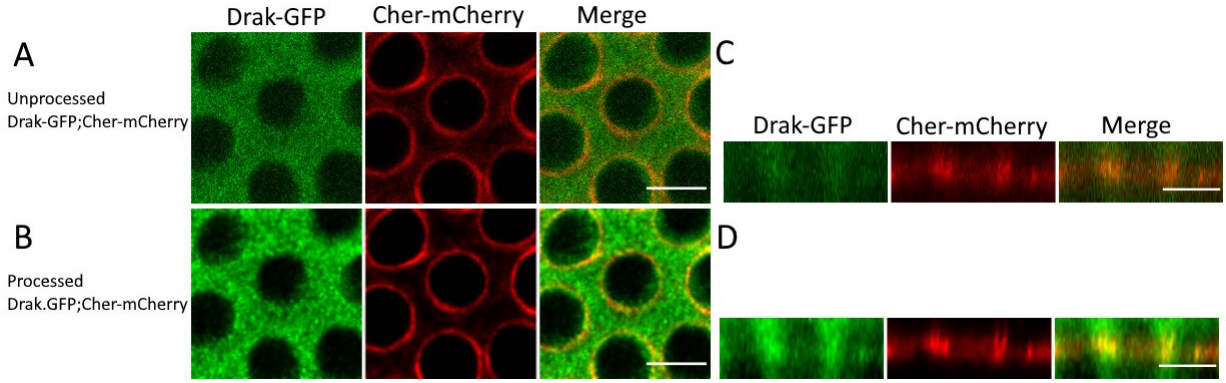

Image of actin front stack from raw unprocessed images and deconvoluted images. Confocal microscopy of Drak-GFP;Cher-mCherry actin front where (A) Unprocessed image from the top view. (B) Processed deconvoluted image from the A. (C) Unprocessed cross-section view of the actin front and (D) processed cross-section view. Top view projection is the same as presented on the cross-section view. Stack size was 5.012 µm. Front distance from the cortex ~7.8 µm. The PSF refraction index was set to 1.33 with other Leica settings as default. Scale bar was set to 5 µm.

APPENDIX 2 DECONVOLUTION EFFECT ON PCC ANALYSIS

The unprocessed scatterplots yielded limited informative. The top view depicted a scattering of pixels in a seemingly irregular distribution. After deconvolution, scatterplots provided more information, showing correlations and improved signal-to-noise ratio. The deconvolution affected the PCC values, which displayed noticeable increase in both fly lines upon image processing.

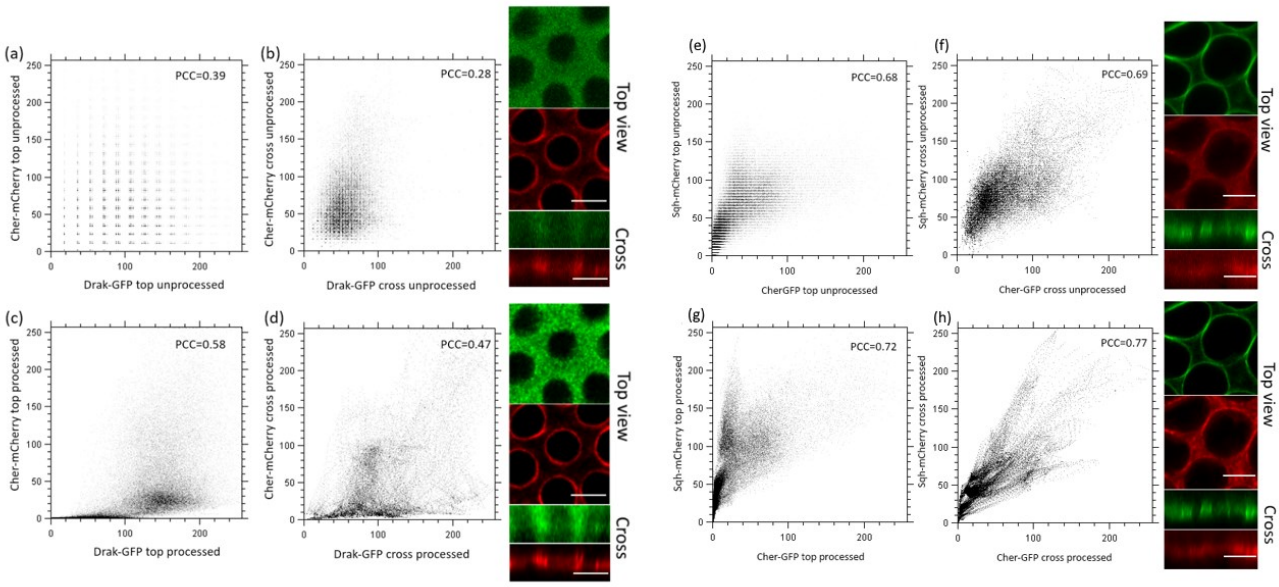

Unprocessed and deconvoluted scatterplots and images. On the left: Drak-GFP;Cher-mCherry. On the right: Cher-GFP;Sqh-mCherry. On top left Drak-GFP;Cher-mCherry unprocessed scatterplot from top view (a) and cross-section view (b). Below Drak-GFP;Sqh-mCherry processed scatterplots from top (c) and cross-section (d). On top right, Cher-GFP;Sqh-mCherry unprocessed scatterplot from top view (e) and cross-section view (f). Below Cher-GFP;Sqh-mCherry processed scatterplots from top (g) and cross-section (h). Corresponding images are presented next to the scatterplots. Top view projection is the same as presented on the cross-section view. For Drak-GFP;Cher-mCherry the stack size 5.012 µm and for Cher-GFP;Sqh-mCherry 5.728 µm. Front distance from the cortex ~7.8 and ~8.9 µm. The PSF refraction index was set to 1.33 with other Leica settings as default. Scale bar was set to 5 µm.

APPENDIX 3. NEGATIVE CONTROL GROUPS

Negative controls Drak-GFP and Cher-mCherry was tested to make sure that the Drak-GFP;Cher-mCherry expressing embryos contained true fluorescence signal (Appendix 3). The expectation for these control groups was the absence of fluorescence in the green or the red channel, given that there is no second probe. Cher-mCherry negative control shows clear visible actin front in the red channel (white arrow), which is absent in the green channel. Top view projection shows regrettably unwanted background noise (yellow arrows). This was also present in the cytosol.

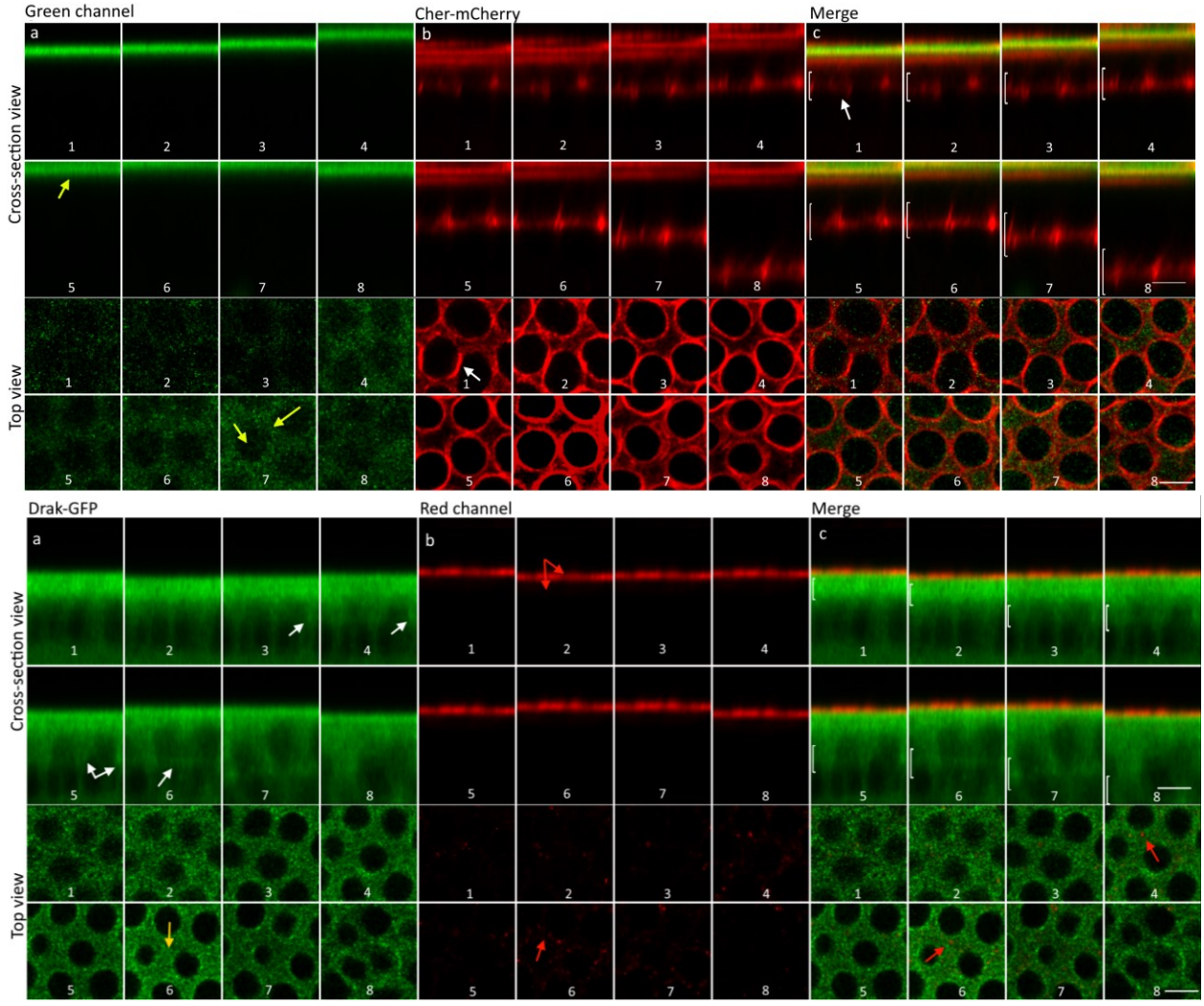

Time-lapse images from controls. On top Cher-mCherry and on below Drak-GFP (B). On the left a) green channel where top panel contains the cross-section view and below the top view. In the middle b) red channel and the third panel c) merged image of the two channels. White bracket in the merge channel indicates the Z-projection corresponding to top view images. Time between the images (1-8) was 5 minutes. Scale bar was set to 5 µm.

Similarly, Drak-GFP shows clear signal compared to the red channel that does not show visible actin front as expected (Appendix 3). However, the Drak-GFP signal was quite weak and hard to distinguish (white arrows). Notably, background noise was observable in both channels. An interesting discovery was the abrupt increase in signal intensity at a specific point within the image (yellow arrow). Similarly, to the Cher-mCherry control, the red channel exhibited unwanted signals from autofluorescence originating from the cortex of the embryo and its surrounding nuclei (red arrows).

APPENDIX 4. DESCRIPIVE STATISTICS

Groups	n			Statistic (PCC)	Std. Error
Cher-mCherry	69	Mean		0.247	0.015
		95% Confidence Interval for Mean	Lower Bound	0.216	
			Upper Bound	0.277	
		Variance		0.016	
		Std. Deviation		0.126	
		Skewness		-0.692	0.289
		Kurtosis		0.970	0.570
Drak-GFP	51	Mean		0.262	0.017
		95% Confidence Interval for Mean	Lower Bound	0.228	
			Upper Bound	0.296	
		Variance		0.015	
		Std. Deviation		0.121	
		Skewness		-0.237	0.333
		Kurtosis		0.139	0.656
Cher-GFP;Sqh-mCherry	69	Mean		0.657	0.017
		95% Confidence Interval for Mean	Lower Bound	0.623	
			Upper Bound	0.691	
		Variance		0.020	
		Std. Deviation		0.142	
		Skewness		-0.650	0.289
		Kurtosis		-0.198	0.570
Drak-GFP;Cher-mCherry	84	Mean		0.559	0.010
		95% Confidence Interval for Mean	Lower Bound	0.539	
			Upper Bound	0.578	
		Variance		0.008	
		Std. Deviation		0.090	
		Skewness		-0.199	0.263
		Kurtosis		-0.948	0.520
Randomized	84	Mean		0.000	0.001
		95% Confidence Interval for Mean	Lower Bound	-0.003	
			Upper Bound	0.002	
		Variance		0.000	
		Std. Deviation		0.013	
		Skewness		-0.100	0.263
		Kurtosis		0.348	0.520

n = number of measurements

APPENDIX 5. NORMALITY TEST

		Kolmogorov-Smirnov[b]			Shapiro-Wilk		
	Groups	Statistic	df	Sig.	Statistic	df	Sig.
Pearson's Correlation Coefficient (PCC)	Cher-mCherry	0.087	69	**0.200***	0.966	69	0.057
	Drak-GFP	0.092	51	**0.200***	0.972	51	0.268
	Cher-GFP;Sqh-mCherry	0.121	69	0.014	0.949	69	**0.007***
	Drak-GFP;Cher-mCherry	0.108	84	0.017	0.968	84	**0.032***
	Randomized	0.073	84	**0.200***	0.983	84	0.331

*. This is a lower bound of the true significance.

b. Lilliefors Significance Correction

APPENDIX 6. INDPENDENT 2-TAILED *T*-TEST

		Levene's Test for Equality of Variances		(Welch's) *t*-test for Equality of Means					Bootstrap[a]	
(I) Groups	(J) Groups	F	Sig.	t	df	Sig. (2-tailed)	Mean Difference (I-J)	Std. Error Difference	Sig. (2-tailed)	
Cher-mCherry	Drak-GFP	0.082	0.775	-0.694	110.097	0.489	-0.016	0.023	0.487	
	Cher-GFP;Sqh-mCherry	1.177	0.280	-17.975	134.172	<0.001***	-0.410	0.023	0.001***	
	Drak-GFP;Cher-mCherry	4.472	0.055	-17.255	120.201	<0.001***	-0.312	0.018	0.001***	
Drak-GFP	Cher-GFP;Sqh-mCherry	1.642	0.203	-16.392	115.412	<0.001***	-0.394	0.024	0.001***	
	Drak-GFP;Cher-mCherry	2.242	0.137	-15.097	83.798	<0.001***	-0.296	0.020	0.001***	
Cher-GFP;Sqh-mCherry	Drak-GFP;Cher-mCherry	10.540	0.001***	4.969	111.040	<0.001***	0.098	0.020	0.001***	
Drak-GFP;Cher-mCherry	Randomized	186.830	0.001***	56.073	86.381	<0.001***	0.559	0.010	0.001***	

*. The difference is significant at the 0.05 level or below

**. The difference is significant at the 0.01 level or below

***. The difference is significant at the 0.001 level or below

a. Bootstrap results are based on 1000 bootstrap samples